Meteoroids detection with the LUMIO lunar CubeSat

Topputo, F.; Merisio, G.; Cervone, A.; Speretta, S.; Menicucci, A.; Turan, E.; Bertels, E.; Vennekens, Johan; Walker, R; More Authors

Important note
To cite this publication, please use the final published version (if applicable).
Please check the document version above.

Meteoroids detection with the LUMIO lunar CubeSat

F. Topputo [a,1], G. Merisio [a,*,2], V. Franzese [a,3], C. Giordano [a,3], M. Massari [a,4], G. Pilato [b,5],
D. Labate [b,6], A. Cervone [c,7], S. Speretta [c,7], A. Menicucci [c,7], E. Turan [c,2], E. Bertels [d,8],
J. Vennekens [e,8], R. Walker [e,9], D. Koschny [e,f,10]

[a] Department of Aerospace Science and Technology, Politecnico di Milano, Via La Masa 34, 20156, Milano, Italy
[b] Leonardo S.p.A., Via delle Officine Galileo 1, 50013, Campi Bisenzio, Firenze, Italy
[c] TU Delft, Kluyverweg 1, 2629 HS, Delft, The Netherlands
[d] ISIS-Innovative Solutions in Space, Motorenweg 23, 2623 CR, Delft, The Netherlands
[e] European Space Research & Technology Centre (ESTEC), ESA, Keplerlaan 1, 2201 AZ, Noordwijk, The Netherlands
[f] TU Munich, Garching, Germany

ARTICLE INFO

ABSTRACT

The Lunar Meteoroid Impacts Observer (LUMIO) is a CubeSat mission to observe, quantify, and characterize the meteoroid impacts on the lunar farside by detecting their flashes. This complements the knowledge gathered by Earth-based observations of the lunar nearside, thus synthesizing global information on the lunar meteoroid environment and contributing to the lunar situational awareness. The goal of LUMIO is to advance our current knowledge of meteoroid models in the solar system. In this work, we present the methodology devised to predict the scientific contribution of LUMIO. Our approach relies on combined modeling and simulation of payload, orbit, and environment. The analyses carried out have been used to drive the design of the LUMIO mission and its payload, the LUMIO-Cam. A payload radiometric model is derived and exploited to assess the quality of the scientific measurements. A dedicated study about straylight rejection is carried out to assess how straylight noise affects LUMIO-Cam measurements. Our results indicate that a 150 mm baffle grants good performance when the Sun angle is between 20° and 90°. Furthermore, the present-day LUMIO mission has the potential to detect more than 6000 impact flashes during the activity peak of the Geminids in 2024 in the range of the equivalent impact kinetic energy at Earth of $[10^{-6}, 10^{-1}]$ kton TNT Equivalent. Compared to previous programmes, LUMIO could refine information and fill the knowledge gap about the meteoroid population in the ranges of the equivalent impact kinetic energy at Earth of $[10^{-6}, 10^{-4}]$ kton TNT Equivalent and $[10^{-4}, 10^{-1}]$ kton TNT Equivalent, respectively.

* Corresponding author.
  E-mail addresses: francesco.topputo@polimi.it (F. Topputo), gianmario.merisio@polimi.it (G. Merisio), vittorio.franzese@polimi.it (V. Franzese), carmine.giordano@polimi.it (C. Giordano), mauro.massari@polimi.it (M. Massari), giuseppe.pilato@leonardocompany.com (G. Pilato), demetrio.labate@leonardocompany.com (D. Labate), a.cervone@tudelft.nl (A. Cervone), s.speretta@tudelft.nl (S. Speretta), a.menicucci@tudelft.nl (A. Menicucci), e.turan@tudelft.nl (E. Turan), e.bertels@isispace.nl (E. Bertels), johan.vennekens@esa.int (J. Vennekens), roger.walker@esa.int (R. Walker), detlef.koschny@esa.int, d.koschny@tum.de (D. Koschny).
  [1] Full Professor.
  [2] PhD Student.
  [3] PostDoc Researcher.
  [4] Associate Professor.
  [5] Payload Engineer.
  [6] Program Manager.
  [7] Assistant Professor.
  [8] Systems Engineer.
  [9] Head of CubeSat Systems Unit.
  [10] Scientist at the Planetary Defence Office, Chair of Astronautics.

1. Introduction

The Earth–Moon system is constantly bombarded by meteoroids of different sizes and velocities, and their numbers are significant. Fragments of asteroids, comets, and major celestial bodies (e. g., Mars and the Moon), constantly encounter the Earth and Moon in their orbits, and impact them as meteoroids. Observations of meteor showers on Earth have been studied for at least 50 years (Ceplecha et al., 1998). Models describing these observations can be useful in, e. g., predicting when the next large meteoroid will impact the Earth itself or the small-meteoroid flux that deteriorates space equipment. As meteoroids originate from asteroids and comets other than major bodies like the Moon and Mars, meteoroid models can also be used to understand the spatial distribution of those objects near the Earth–Moon system (Ceplecha et al., 1998). By observing the lunar surface impacts, whose flux is similar to that of the Earth, we could obtain detailed information regarding their magnitudes, velocities, temporal, and spatial distributions. This information can be used to increase confidence of meteoroid models, to validate existing lunar impact models, to contribute to lunar seismology studies and interior modeling, and to initiate a lunar situational awareness programme for future exploration missions (Cahill et al., 2021). A programmatic observation of the lunar surface for impact flash detections and flux observations would be beneficial to help quantifying the threat posed to future human and robotic assets that will inhabit the Moon (over and under the surface) for significant periods of time. Impact flashes, plumes, and craters are all opportunities to enhance the present-day knowledge about the meteoroid environment required to design appropriate hazard mitigation and defensive strategies for a successful new era of lunar exploration (Cahill et al., 2021).

Earth-based optical observations of the light flashes produced by lunar meteoroid impacts have proven useful in the validation and improvement of meteoroid models (Oberst et al., 2012). Conversely to the Earth case where the atmosphere burns the small impactors, the Moon does not have atmosphere, so smaller objects can reach the ground. Additionally, monitoring the Moon for meteoroid impact flashes allows for the observation of larger areas than those covered by traditional surveys of Earth upper atmosphere. Thus, theoretically, more meteoroid impacts can be detected in shorter periods of time if a similar size range is considered (Bellot Rubio et al., 2000).

Earth-based lunar observations are restricted by weather, geometric, and illumination conditions. As such, a lunar spacecraft can improve the detection rate of lunar meteoroid impact flashes, as it would allow for longer monitoring periods. Moreover, if placed close to the Moon surface, a lunar spacecraft could also allow for the detection of meteoroids smaller than millimeters (Koschny and McAuliffe, 2009). The current trend in spacecraft miniaturization technologies is enabling CubeSat missions in lunar environment. Space agencies like NASA, ESA, and JAXA are planning CubeSat missions for lunar scientific investigations such as Lunar Flashlight (Cohen et al., 2020), VMMO (Walker et al., 2018), EQUULEUS (Oguri et al., 2020), and LUMIO (Cipriano et al., 2018).

LUMIO is a CubeSat mission to observe, quantify, and characterize meteoroid impacts on the lunar farside by detecting their flashes to provide global information on the lunar meteoroid environment and contribute to lunar situational awareness (Walker et al., 2018). It complements ground-based observations on the lunar nearside (Avdellidou et al., 2021; Liakos et al., 2020; Yanagisawa et al., 2021; Jenniskens et al., 2016a,b,c; Ortiz et al., 2006, 2015; Madiedo et al., 2015; Suggs et al., 2014). LUMIO was awarded winner of ESA's competition "Lunar CubeSat for Exploration", and as such it is being considered for implementation.[11] The Phase 0 study was carried out in 2017; an

independent mission assessment by ESA followed in 2018; the Phase A study has been carried out in 2020–2021 under ESA's General Support Technology Programme (GSTP). The mission implements the latest technologies to enable CubeSats as viable machines for deep space science and exploration (Cervone et al., 2022; Merisio et al., 2020).

In this paper, we present the scientific contribution of LUMIO. The scientific return of the mission is compared against those of previous programmes to highlight how LUMIO can potentially refine the known data in the equivalent impact kinetic energy at Earth of $[10^{-6}, 10^{-4}]$ kton TNT Equivalent, and how it can fill the knowledge gap for the flux density in the range $[10^{-4}, 10^{-1}]$ kton TNT Equivalent. The methodology used to predict the scientific contribution is also discussed. It integrates information about the payload, the operative orbit, and the lunar meteoroid environment to conduct analyses on the detection of meteoroid impacts. Effort is put to the payload radiometric model and the considered noise sources affecting the measurements: straylight (due to ghosts, contamination, and roughness), the surface background noise of the Moon, dark current, read-out noise, off-chip noise, and quantization noise. The operative orbit is a quasi-periodic halo about Earth–Moon L_2 (Cipriano et al., 2018). The lunar meteoroid environment is simulated according to the model in Merisio and Topputo (2022). An assessment about the performance degradation due to straylight noise is carried out. Eventually, results of the integrated payload, orbit, and environment (POE) analysis are presented. In the latter, a Monte Carlo analysis is carried out to predict the expected number of detected meteoroid impacts, together with their energy and temporal distribution.

The remainder of the paper is organized as follows. In Section 2, an overview of the LUMIO mission is provided. The modeling of the lunar meteoroid environment is outlined in Section 3. The payload radiometric model is detailed in Section 4. Results from the radiometric analysis and the integrated POE analysis follow in Section 5 and Section 6, respectively. Concluding remarks are given in Section 7.

2. LUMIO lunar CubeSat

LUMIO is a CubeSat that will be placed on a halo orbit at Earth–Moon L_2 to observe, quantify, and characterize meteoroid impacts on the lunar farside. The LUMIO mission is conceived to address the following issues:

- **Science question**. What are the spatial and temporal characteristics of meteoroids impacting the lunar surface?
- **Science goal**. Advance the understanding of how meteoroids evolve in the cislunar space by observing the flashes produced by their impacts with the lunar surface.
- **Science objective**. Characterize the flux of meteoroids impacting the lunar surface.

LUMIO wants to quantify the luminous energy of meteoroid impacts to the Moon in the equivalent impact kinetic energy range at the Earth from 10^{-6} to 10^{-4} kton TNT Equivalent. In fact, observations reported in the literature have significant error margins and also a set of discrepancies (Ortiz et al., 2015; Suggs et al., 2014). Additionally, the mission aims to detect new meteoroid impacts on the Moon in the equivalent kinetic energy range from 10^{-4} to 10^{-1} kton TNT Equivalent. Indeed, no events have ever been recorded in the latter energy range (Ortiz et al., 2015; Suggs et al., 2014).

Fig. 1 shows the potential scientific contribution of the LUMIO CubeSat compared to data of previous programmes (Suggs et al., 2014). The comparison shows how LUMIO will detect new impacts in the range at higher energy (green background) and will contribute to refine the knowledge in the lower energetic range (light blue background). Some of the impacts in the high-energy range cannot be successfully detected by the LUMIO-Cam (yellow diamonds in the plot). They saturate both detectors due to their high energy.

The list of top-level objectives of LUMIO is shown in Table 1, while the lists of mission and technological demonstration objectives are presented in Tables 2 and 3, respectively.
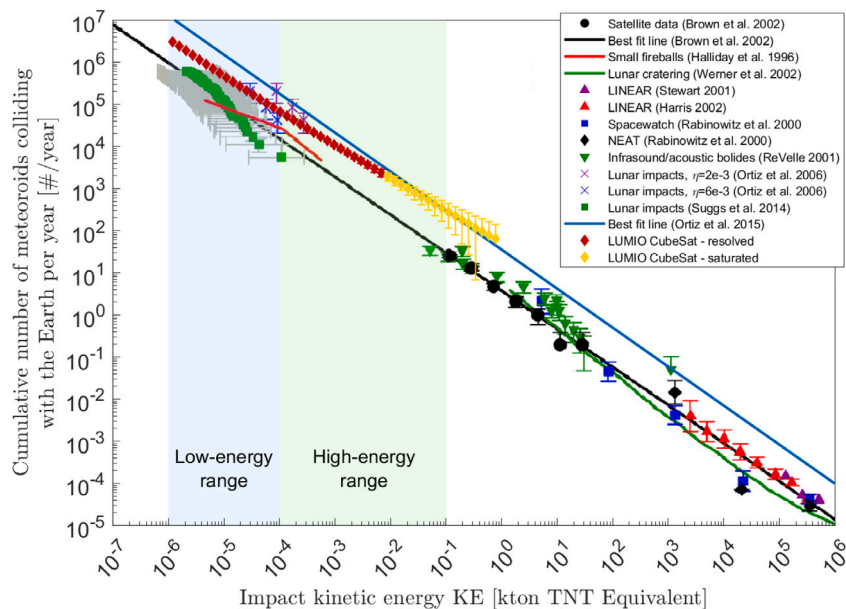
Fig. 1. Comparison of the estimated LUMIO lunar CubeSat scientific return with the scientific return of previous programmes. Some points do not show the bottom bar because they reach negative values and the plot is in logarithmic scale. Logarithmic scale plot. The plot is an elaborated version of Figure 9 in Suggs et al. (2014), courtesy of Dr. R. M. Suggs, Dr. D. E. Moser, Dr. W. J. Cooke, and Dr. R. J. Suggs.

Table 1
Top-level objectives.

ID	Objectives
TLO.01	To perform remote sensing of the lunar surface and measurement of astronomical observations not achievable by past, current, or planned lunar missions.
TLO.02	To demonstrate deployment and autonomous operation of CubeSats in lunar environment, including localization and navigation aspects.
TLO.03	To demonstrate miniaturization of optical instrumentation and associate technology in lunar environment.
TLO.04	To perform inter-satellite link to a larger Lunar Orbiter for relay of data and for TT&C.

Table 2
Mission objectives.

ID	Objectives
MO.01	To conduct observations of the lunar surface in order to detect meteoroid impacts and characterize their flux, magnitudes, luminous energies, and sizes.
MO.02	To complement observations achievable via ground-based assets in space, time, and quality in order to provide a better understanding of the meteoroid environment.

Table 3
Technological objectives.

ID	Objectives
TDO.01	To perform autonomous navigation experiments by using images of the Moon.
TDO.02	To demonstrate CubeSat trajectory control capabilities into lunar environment.
TDO.03	To demonstrate the use of miniaturized optical payload in lunar environment.
TDO.04	To demonstrate the use of miniaturized technologies into lunar environment.
TDO.05	To demonstrate the use of miniaturized propulsion systems in lunar environment.
TDO.06	To perform autonomous, high-performance on-board payload data processing.

2.1. Overview of the mission

The mission utilizes a 12-unit CubeSat of the so-called XL form-factor, i. e., 12 blocks of $12.2 \times 12.2 \times 12.2 \, cm^3$ size (Puig-Suari et al., 2001; Poghosyan and Golkar, 2017) that carries the LUMIO-Cam, an optical instrument capable of detecting light flashes in the visible spectrum to continuously monitor and process the scientific data (Merisio et al., 2020). The mission implements a novel orbit design (Cipriano et al., 2018) and commercial off-the-shelf (COTS) CubeSat technologies, to serve as a pioneer in demonstrating how CubeSats can become a viable tool for interplanetary science and exploration (Cervone et al., 2022). The design of the LUMIO CubeSat platform is shown in Fig. 2.

The mission will be divided in several phases: launch, Earth–Moon transfer, parking, transfer to the operative orbit, operative, and end-of-life. LUMIO is expected to accomplish its scientific objectives during the operative phase. The nominal duration of the phase is 1 year, and it is subdivided in two periodical cycles: (i) the *science cycle*, during which the scientific data are continuously acquired, processed on board and compressed, and (ii) the *navigation & engineering* cycle, during which radiometric navigation based on direct-to-Earth (DTE)
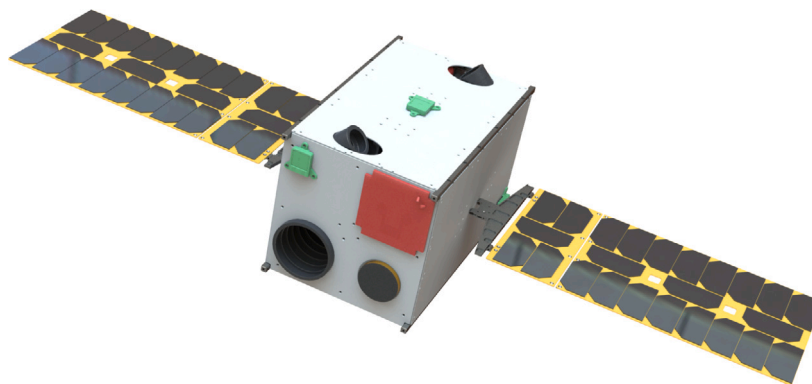
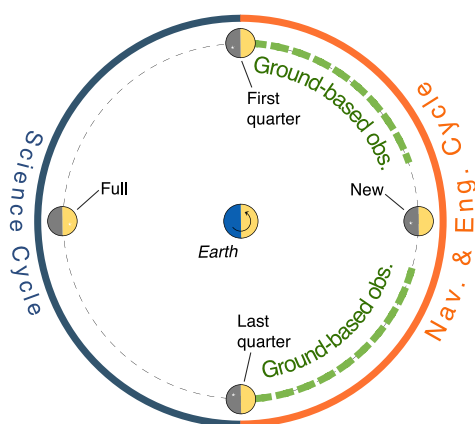**Fig. 2.** LUMIO lunar CubeSat configuration.

Fig. 3. Science and navigation & engineering cycles in relation to Moon phases.

link is performed (in parallel with the demonstration of an autonomous optical navigation experiment using the LUMIO-Cam (Franzese et al., 2019)), and station keeping and wheel desaturation maneuvers are conducted. With reference to Fig. 3, the science cycle takes place during the portion of the lunar cycle when the illumination of the Moon allows for scientific observations (solid blue line), while the navigation & engineering cycle will take place when scientific observations of the lunar farside are not possible (solid orange line).

2.2. Operative orbit

A quasi-periodic halo orbit about Earth–Moon L_2 is the designated operative orbit for LUMIO. The selection of the operative orbit is the result of a thorough trade-off analysis performed during the Phase 0 study (Cipriano et al., 2018). According to the assumed timeline of the mission, the operative phase is expected to start on 21 March 2024, and to end on 22 March 2025. Fig. 4 shows the top and lateral views of the LUMIO quasi-halo orbit. The trajectory is represented in the Earth–Moon roto-pulsating frame in dimensionless coordinates. The ranges of LUMIO from the Moon and the Earth are plotted in Fig. 5. The range to the Moon spans between 36 000 km and 86 000 km, while the range to the Earth spans between 380 000 km and 470 000 km.

2.3. LUMIO-cam payload

The LUMIO-Cam is a custom instrument. It implements two channels, one in the visible and one in the near-infrared, each equipped with a charged-coupled device (CCD) having 1024×1024 active pixels, associated to an optics with a field of view of 6° and 150 mm focal length. After the optics, a dichroic beam splitter divides the incoming signal

into two channels. Mounting two channels allows validating observed flashes directly on board, as well as estimating the equivalent black body temperature characteristic of the plumes they generate (Bonanos et al., 2018). The LUMIO-Cam design is shown in Fig. 6.

The peculiarity of the LUMIO-Cam is the presence of two channels, the visible spectrum channel (VIS) and the near-infrared wavelength range channel (NIR). The incoming light is split at 820 nm by means of a dichroic. Each focal plane assembly includes a CCD detector, at the present-day the baseline is the CCD201-20[12] of e2V L3Vision™. The selected detector is a frame-transfer CCD. In frame-transfer CCDs the image array and the storage array are divided into two distinct areas. Thus, a frame-transfer CCD can operate continuously. After the signal is measured, the CCD output is sampled and digitized by the 14-bit A/D converter AD9240.[13] The LUMIO-Cam takes pictures with exposure time Δt_{exp} = 66 ms, meaning that the payload works at 15 fps. The entrance baffle is 150 mm long and it assures that no direct sunlight hits the first lens at sun angles larger than 20 deg.

The spectrum range in which the LUMIO-Cam is sensitive is $[450, 950]$ nm. The signals detected by VIS and NIR channels are in the bandwidths $[450, 820]$ nm and $[820, 950]$ nm, respectively. The aperture diameter is computed through the relation $F_\# = FL/D$, where $F_\# = 2.5$ and the focal length FL $= 127$ mm. D is equal to 50.8 mm. The quantum efficiency (QE) curve of the selected detector is shown in Fig. 7. According to the manufacturer, the low noise gain of the CCD detector can be varied from 1× to over 1000×. In this radiometric analysis it is assumed that the gain may assume any of the integer values within the range $[1, 1000]$. The complete list of the LUMIO-Cam specifics is presented in Table 4.

Impact flashes are validated on-board thanks to the presence of the two detectors that prevent detecting false positives due to galactic cosmic rays. Frame tiles of confirmed flashes are downloaded in batch during the next navigation & engineering cycle, within 15 days after the end of the science cycle. The meteoroid flux (and thus the acquired payload data) is not constant over the year, consequently variations in the data transmitted to Earth have to be considered (Cervone et al., 2022).

An estimation of the scientific data budget has been assessed assuming the following scientific products to be downloaded: picture tiles of 50×50 pixels (frames cropped around the flash); 5 tiles saved per impact; 2 channels working synchronously (tiles from both channels downloaded); 2 bytes (16 bits) per pixel. For what concerns the overall scientific data budget, approximately 15 Gbit of data are expected to be produced for an operative phase lasting 1 year.

Table 4
LUMIO-Cam specifics.

Specific	Symbol	Value
CCD detector[b]	ID	e2v CCD201–20
Focal length[b]	FL	127 mm
F number[c]	$F_\#$	2.5
Aperture diameter[c]	D	50.80 mm
Baffle length[c]	l_{baffle}	150 mm
Sun exclusion angle[c]	$\phi_\odot$	20 deg
Field of view[b]	FOV	6 deg
Sensitivity range[c]	$[\lambda_1, \lambda_2]$	[450, 950] nm
Dichroic wavelength[c]	λ_{dic}	820 nm
Active pixels[a]	N_{pix}	1024×1024 pixel
Pixel size[a]	d_{pix}	13.3×13.3 µm²
Exposure time[b]	Δt_{exp}	66 ms
Frame per second[b]	FPS	15 fps
Low noise gain[a]	G	[1, 1000]
Excess noise factor[a]	F	$\sqrt{2}$
Charge handling capacity[a]	C	80 ke⁻ pixel⁻¹
Charge handling capacity of multiplication register[a]	C_{MR}	730 ke⁻ pixel⁻¹
Readout frequency[b]	f_{rout}	15 MHz
Maximum readout frequency[a]	$f_{rout,max}$	20 MHz
Readout noise[ad]	$\sigma_{RON,0}$	<1 e⁻ rms
Off-chip noise[a]	off$_n$	20×10^{-9} V/$\sqrt{HZ}$
Output amplifier responsivity[a]	OAR	1.4 µV$(e^-)^{-1}$
analogue to digital (A/D) converter bit number[b]	N_{bits}	14 bit

[a]See Footnote 12.
[b]Heritage of Phase 0 study.
[c]Phase A study.
[d]Evaluated at $f_{rout} = 1$ MHz and $G = 1000$.

(a) Top view, xy-plane. (b) Lateral view, xz-plane. (c) Lateral view, yz-plane.
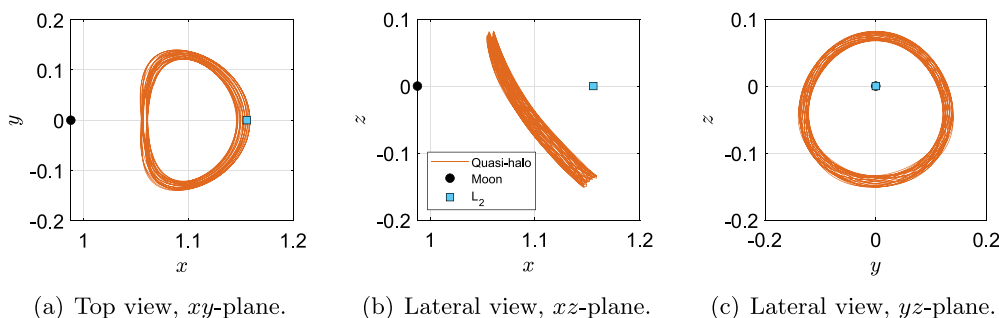
Fig. 4. LUMIO quasi-halo orbit about Earth–Moon L_2.
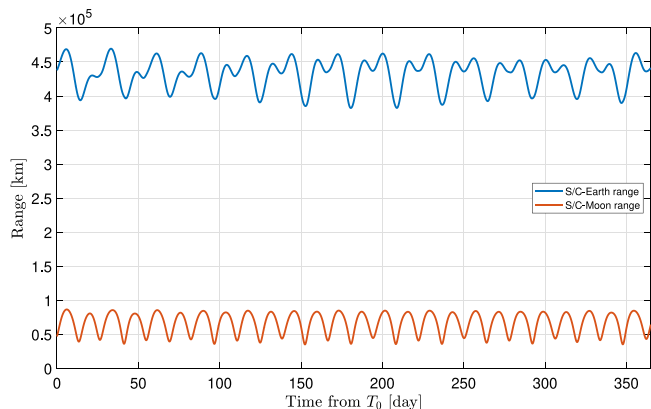

Fig. 5. LUMIO distances from the Moon and the Earth during the operative phase.

3. Lunar meteoroid environment dataset

To simulate the lunar meteoroid environment, a dedicated tool named Meteoroid Gun (MeGun) has been used. The tool computes

dataset of the lunar meteoroid environment scenarios required to perform the radiometric analysis, the integrated POE analysis, and the estimation of the scientific return of the LUMIO mission. It implements the modeling of the lunar meteoroid environment discussed in Merisio and Topputo (2022). Such model allows reproducing scenarios of the environment with a stochastic approach, generating each meteoroid individually.

The basis of the model resides in the experimental observations of fireballs, impact flashes, and meteors. A stochastic approach is exploited since observations are affected by uncertainties on measurements and forecasting. Indeed, meteoroid streams are dynamic entities, which are subjected to yearly variation in the flux and in the maximum peak activity (Hughes, 1987).

The model requires as inputs the time span to be simulated and a threshold on the minimum impact kinetic energy of meteoroids. It returns a set of descriptors for each impact. Both meteoroid streams and the sporadic background are modeled. The model relies on a comprehensive catalog about meteoroid streams and the sporadic background built harmonizing information from the IAU's Meteoroid Data Center (MDC) database[14] and from catalogs found in the literature (Jenniskens, 1994; Jenniskens and Jenniskens, 2006; Jenniskens et al.,

---

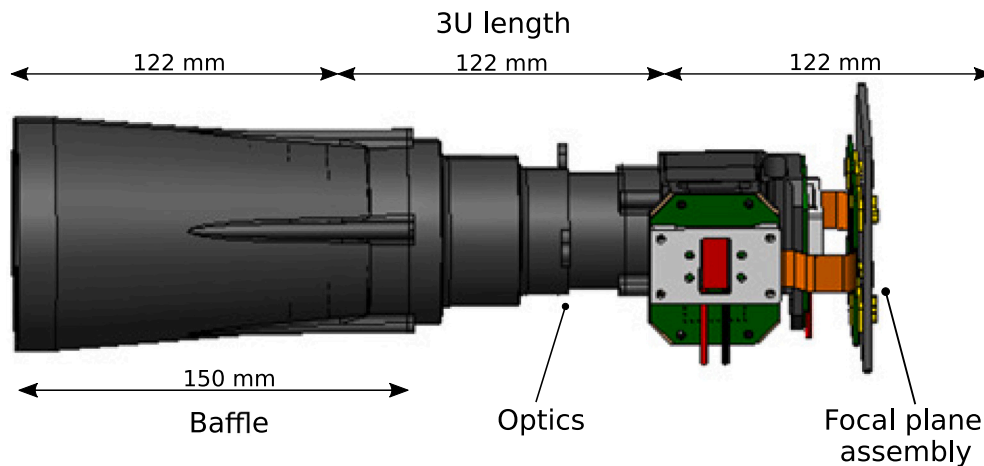[14] https://www.ta3.sk/IAUC22DB/MDC2007/ [last accessed March 1, 2022].
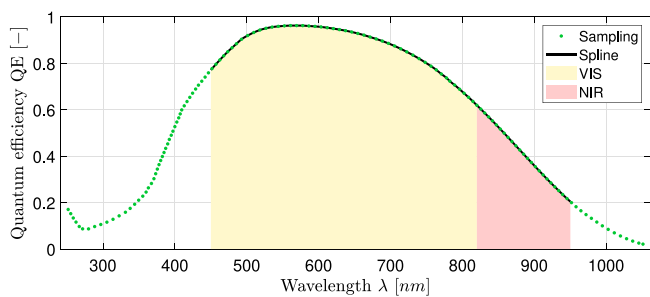
Fig. 6. LUMIO-Cam overall architecture.

Fig. 7. QE curve of CCD201-20 detector. The curve has been digitized starting from the original plot found in the detector datasheet. The bandwidths received by VIS and NIR channels are highlighted with different colors. Sampling points are represented by point markers, while the curve is the result of a spline interpolation.

2016b; Babadzhanov and Kokhirova, 2009; Brown et al., 2008, 2010; Jenniskens et al., 2016a,c); see Merisio and Topputo (2022) for more details.

4. Modeling of the payload

4.1. Radiometric model

The purpose of the radiometric analysis is to assess the performance of the LUMIO-Cam. The assessment is performed evaluating the signal-to-noise ratio (SNR) of impact flashes of meteoroids in the kinetic energy range of interest and check that it is over a certain threshold to grant their detection. The light curve of the impact flash is modeled as the one of a black body emitting for a given duration with a constant equivalent black body temperature computed as in Merisio and Topputo (2022). The SNR is defined as (Raab, 2002)

$$\text{SNR} = \frac{s_i}{\sigma} \tag{1}$$

where s_i is the signal in e^- (number of electrons) of a generic source of interest while σ is the Poisson noise in e^- rms (root-mean-square) associated with all signals collected by the detector. Note that s_i and σ refer to a single pixel. The Poisson noise of a source i is given by Raab (2002)

$$\sigma_i = \sqrt{s_i} \tag{2}$$

while the total Poisson noise is (Raab, 2002)

$$\sigma = \sqrt{\sum_i \sigma_i^2} = \sqrt{\sum_i s_i}. \tag{3}$$

4.1.1. Impact flash duration in LUMIO-cam frames

A flash may occur at any time, which means that the starting times of an impact flash and its photographic frame in general do not coincide. Such mismatch is taken into account when computing the SNR. The two CCDs work in parallel and are electronically synchronized (Cervone et al., 2022). Tests carried out by the payload provider confirmed that the difference in the synchronization between frames of different channels is negligible compared to the exposure time of the LUMIO-Cam. Therefore, the channels are considered perfectly synchronized and the flash duration in simultaneous frames is exactly the same. Nevertheless, the flash duration in the two different wavelength ranges of the LUMIO-Cam is expected to be different. In fact, the visible part fades quicker than the near-infrared one according to the knowledge acquired from ground-based observations carried out by the NELIOTA programme (Liakos et al., 2020; Bonanos et al., 2018, 2015) and reported in the NELIOTA dataset.[15] Nonetheless, in this work the flash duration is assumed independent from the wavelength.

Starting times of flashes are not known a priori because a clock linking the lunar meteoroid environment simulations and the payload model is not implemented. Instead, they are randomly drawn. The flash duration in each individual frame is then deduced from the exposure time Δt_{exp} and the impact flash duration modeled as in Merisio and Topputo (2022). When a flash lasts more than one frame, only the first and second frames are retained for the radiometric analysis. Frames after the second are discarded because the resulting SNR would not be reliable. The reason is that the temperature of the plume is assumed constant and equal to the average equivalent black body temperature over the flash duration (Merisio and Topputo, 2022). The longer the flash duration (longer than $100\,\text{ms}$), the less reliable the estimation of the SNR. The latter is because the ejecta plume cooling is not modeled.

A random number ϵ is drawn from a uniform distribution bounded in $[0, 1]$. Next, the flash duration in the first frame τ_1 is computed as

$$\begin{cases} \tau_1 = \epsilon \Delta t_{\text{exp}} & \text{if} \quad \tau \geq \epsilon \Delta t_{\text{exp}} \\ \tau_1 = \tau & \text{if} \quad \tau < \epsilon \Delta t_{\text{exp}} \end{cases} \tag{4}$$

while the duration in the second frame τ_2 is

$$\begin{cases} \tau_2 = \tau - \tau_1 & \text{if} \quad 0 \leq \tau - \tau_1 \leq \Delta t_{\text{exp}} \\ \tau_2 = \Delta t_{\text{exp}} & \text{if} \quad \tau - \tau_1 > \Delta t_{\text{exp}}. \end{cases} \tag{5}$$

A schematic representation of the procedure is shown in Fig. 8 where three possible cases are identified.

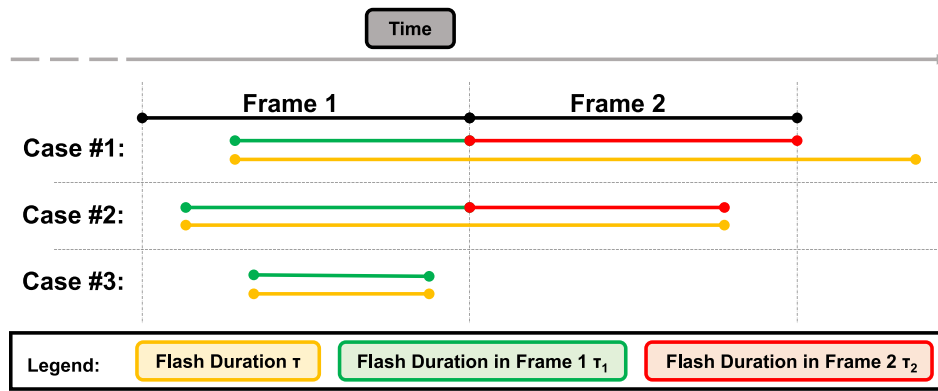[15] https://neliota.astro.noa.gr/DataAccess [last accessed March 1, 2022].

Fig. 8. Schematic representation of flash duration computation within the first and second frames. Three different cases are identified.

4.1.2. Signal peak location

Without loss of generality, the impact is assumed to occur close to the sub-satellite point. As a consequence, the signal peak is contained in the central pixel of the LUMIO-Cam CCD detectors because of the continuous pointing towards the center of the Moon foreseen by the mission during the science cycles. Regarding the location of the signal peak within the pixel, three significant cases are identified. Firstly, the *case a* in which the peak location is exactly at the center of the pixel and the impact flash is completely contained within 1 pixel. In this case, the spread fraction is equal to the unity. Then, the *case b* in which only half of the impact flash point spread function (PSF) is contained within the pixel. This is expected to be the most common case, the spread fraction being equal to 1/2. Finally, the *case c* in which the peak location coincides with one of the four pixel corners, and the spread fraction is 1/4.

4.1.3. Impact flash signal

After a meteoroid impacts with the lunar surface, a plume made of ejecta material is generated by the impact itself. Such plume emits radiation, which can be detected as an impact flash. The signal coming from the impact flash is computed based on the equivalent black body temperature associated to the plume simulated. The radiating plume cools down after the impact, hence, the equivalent black body temperature decreases in time (Bouley et al., 2012). Nonetheless, the cooling process is not modeled and the temperature is assumed constant with time and equal to the average equivalent black body temperature of the plume over the impact flash duration (Merisio and Topputo, 2022). Since the average temperature is the one assumed constant, our results are expected to match those accounting for a non-constant temperature. We assumed a constant temperature equal to the average one to recover the impossibility to model the correct temperature evolution for each projectile. Indeed, the cooling process is currently not completely understood, and a clear correlation between the temperature evolution with other quantities (e. g., the mass or the energy of the projectile) is not available in the literature (Liakos et al., 2020). Such limitation is very likely linked to the poor knowledge of heat capacity and thermal conductivity of both meteoroids and lunar soil which strongly affect the temperature evolution (Liakos et al., 2020).

To compute the signal, we have taken into account: the sensitive spectrum range of the LUMIO-Cam, the dichroic wavelength, the aperture diameter, the fraction of polychromatic ensquared energy in 1 pixel, the attenuation effects of the optics (bulk absorption, real coating transmission, dichroic lens transmission), the QE of the equipped CCD detector, the gain of the LUMIO-Cam, the distance from the impact location, and the impact dynamics (equivalent black body temperature of the plume, plume area, and flash duration). These characteristics are detailed in the following paragraphs.

Fraction of polychromatic ensquared energy in 1 pixel. The fraction of polychromatic ensquared energy in 1 pixel used to assess the radiometric analysis is $f_{\text{ensq}} = 0.89$. That corresponds to the ensquared energy at the 1 pixel half width distance from the centroid (see Fig. 9).

Attenuation effects of the optics. The presence of optics causes some attenuation effects acting on the signal. The transmissivity defines the number of photons that pass through the optics. The curve describing the transmissivity of the optics at the wavelengths corresponding to the sensitive spectrum range of the camera is shown in Fig. 10. The curve takes into account how bulk absorption and real coating affect the transmissivity $\xi(\lambda)$ of the LUMIO-Cam. An additional loss due to the dichroic lens affects the performance of the LUMIO-Cam, to account for that a dichroic transmissivity η_{dic} equal to 0.9 is assumed.

Number of electrons. The QE is used to convert the photons number at a given wavelength into a number of electrons. The flux of photons at a given wavelength per unit time is obtained dividing the spectral emissive power by the energy of the photon. The formula of the photon energy is

$$E_\gamma(\lambda) = \frac{hc}{\lambda} \tag{6}$$

where γ is the notation used when referring to photons, h is Planck's constant, c is the speed of light in vacuum, and λ is the wavelength of interest.

The flux of photons is converted into a flux of electrons at a given wavelength per unit time by means of

$$N_{e^-}(\lambda, T) = \frac{L(\lambda, T)}{E_\gamma(\lambda)} \text{QE}(\lambda)\xi(\lambda)\eta_{\text{dic}}f_{\text{ensq}} \tag{7}$$

where $L(\lambda, T)$ is the spectral emissive power defined as in Merisio and Topputo (2022). The flux of electrons per unitary interval of wavelength per unit time for any black body is obtained inserting in Eq. (7) the temperature of that black body. In Eq. (7), $N_{e^-}(\lambda, T)$ is measured in $\text{e}^- \, \text{m}^{-2} \, \text{m}^{-1} \, \text{s}^{-1}$.

Impact dynamics. The impact dynamics quantities needed to compute the SNR are retrieved simulating the meteoroid environment (Merisio and Topputo, 2022). It is assumed that meteoroids impact the Moon with a random velocity drawn from a truncated Gaussian distribution with mean equal to $17 \, \text{km s}^{-1}$ (Oberst et al., 2012; Madiedo et al., 2015) (average value of the sporadic population that includes the most meteoroids), standard deviation equal to the 10% of the mean, and bounded in $[10.2, 73.8] \, \text{km s}^{-1}$ (Cipriano et al., 2018).

Computation of the flash signal. The impact flash signal s_{imp} is

$$\begin{aligned}
s_{\text{imp}} &= \frac{A_{\text{oa},\perp}}{A_d} A_p \tau_i \int_{\lambda_1}^{\lambda_2} N_{e^-}(\lambda, T_{\text{imp}}) \text{d}\lambda \\
&= \frac{D^2 \cos(\theta)}{4 \, f d_{\text{imp}}^2} A_p \tau_i \int_{\lambda_1}^{\lambda_2} N_{e^-}(\lambda, T_{\text{imp}}) \text{d}\lambda
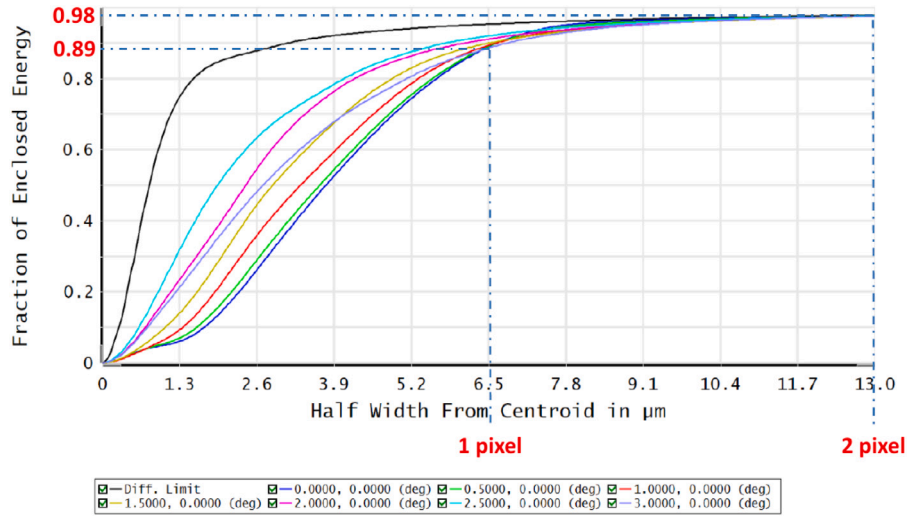\end{aligned} \tag{8}$$

Fig. 9. Fraction of polychromatic ensquared energy. Two significant half width distances from the centroid are highlighted. The first corresponding to the 1 pixel distance and the second corresponding to the 2 pixels distance. The one of interest is the 1 pixel distance.
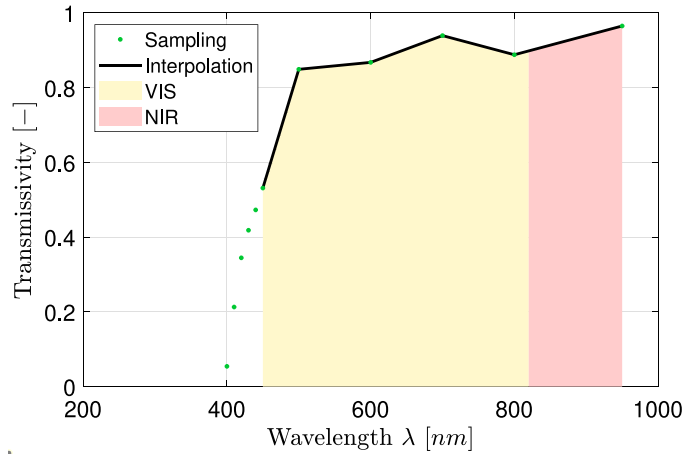

Fig. 10. Transmissivity of the LUMIO-Cam optics, dichroic contribution not included. The bandwidths received by VIS and NIR channels are highlighted with different colors. Sampling points are represented by point markers, while the curve is the result of a piece wise linear interpolation.

where $A_{\mathrm{oa},\perp} = \pi D^2 \cos(\theta)/4$ is the surface of optics aperture perpendicular to the vector pointing towards the impact location, $A_d = f\pi d_{\mathrm{imp}}^2$ is the area used to scale the signal at observer distance, D is the aperture diameter, θ is the angle between the boresight direction and the vector pointing towards the impact location, which is zero (the impact is assumed to happen at the sub-satellite point), $f = 3\pi$ is the anisotropy degree used in Merisio and Topputo (2022), τ_i is the flash duration in the photographic frame considered, A_p is the radiating plume area, and $[\lambda_1, \lambda_2]$ is the domain in which the function $N_{e^-}(\lambda, T)$ is integrated. The integration domain is different for VIS and NIR channels due to the dichroic.

4.2. Noise sources

The noise sources taken into account to compute the SNR are: the noise associated with the impact signal itself σ_{imp} (or photon shot noise), the Moon surface background noise $\sigma_{\mathbb{C}}$, the dark current (DC) (or internal noise of the CCD) σ_{DC}, the read-out noise (RON) of the CCD σ_{RON}, the off-chip noise (OCN) of the CCD σ_{OCN}, the quantization noise (QN) introduced by the A/D converter σ_{QN}, and the straylight noise σ_{sl} (considered in a dedicated analysis). The noise of the signal itself is $\sigma_{\mathrm{imp}} = \sqrt{s_{\mathrm{imp}}}$. The computation of the other noise sources is presented in the following paragraphs.

Surface background noise of the Moon. The signal coming from Moon surface background is

$$s_{\mathbb{C}} = \frac{A_{\mathrm{oa},\perp}}{A_d} A_{\mathrm{GSD}} \Delta t_{\exp} \int_{\lambda_1}^{\lambda_2} N_{e^-}(\lambda, T_{\mathbb{C}}) \mathrm{d}\lambda \qquad (9)$$

where $A_d = 2\pi d^2$ is the scaling factor to compute the flux at observer distance,[16] d is the distance from LUMIO to the impact location, A_{GSD} is the area of the Moon surface corresponding to the instantaneous field of view (IFOV) at distance d of the pixel containing the flash signal, and the subscript GSD refers to the acronym ground sampling distance (GSD). In $A_{\mathrm{oa},\perp} = \pi D^2 \cos(\theta)/4$, θ is the same as in Eq. (8), which is zero since the impact occurs at nadir. Then, $\Delta t_{\exp}$ is the integration time of the camera and $T_{\mathbb{C}} = 150\,\mathrm{K}$ is the assumed Moon's surface temperature. The extremes of integration depend on the LUMIO-Cam channel under consideration.

The impact is assumed to occur at the sub-satellite point and LUMIO is far from the Moon. As a consequence, A_{GSD} may be computed in the planar approximation like

$$A_{\mathrm{GSD}} = \mathrm{GSD}^2 = \left(\frac{h\, d_{\mathrm{pix}}}{\mathrm{FL}}\right)^2. \qquad (10)$$

---

[16] The signal is emitted from the surface, then, 2π is used.

Here, h is the CubeSat altitude. A_{GSD} is computed in the planar approximation, then $h = d$. As a consequence, the surface background signal does not depend on the impact distance. The corresponding Poisson noise is given by $\sigma_{\mathbb{C}} = \sqrt{s_{\mathbb{C}}}$.

Dark current noise. The internal noise of the CCD detector is obtained following the producer guidelines.[17] The dark current signal is computed as

$$s_{DC} = 1.5 \; \frac{d_{pix}^2 \Delta t_{exp}}{q} \; S_d \; 10^{-5} \tag{11}$$

where a 50% margin is introduced by the factor 1.5, q is the electron charge, S_d is the typical surface dark signal in $nA\,cm^{-2}$, and the coefficient 10^{-5} is used to convert S_d in $A\,m^{-2}$. S_d is given by

$$S_d = \alpha S_s + S_b \tag{12a}$$

$$S_s = 122 \; T_{det}^3 \; e^{-\frac{6400}{T_{det}}} \tag{12b}$$

$$S_b = 3.3 \times 10^6 \; T_{det}^2 \; e^{-\frac{9080}{T_{det}}} \tag{12c}$$

where $\alpha = 0$ if CCD is operated in inverted mode (IMO) like for the LUMIO-Cam,[18] and T_{det} is the temperature of the detector in K. A detector temperature $T_{det} = 293.15\,K$ is assumed. The Poisson noise is retrieved from the signal through Eq. (2).

Read-out noise. The mathematical expression of RON is

$$\sigma_{RON} = \sigma_{RON,0} \; \sqrt{\pi f_{rout}} \tag{13}$$

where f_{rout} is the readout frequency, to be inserted in MHz, and $\sigma_{RON,0} = 1$ is the maximum value of RON when $f_{rout} = 1\,MHz$ (see Table 4). The readout frequency depends on the exposure time as

$$f_{rout} = \frac{N_{pix}}{\Delta t_{exp}} \tag{14}$$

where $N_{pix} = 1024^2 pixel$ is the total number of CCD pixels.

Off-chip noise. The expression of the OCN is (Cipriano et al., 2018)

$$\sigma_{OCN} = \frac{off_n}{OAR} \sqrt{\pi f_{rout}}. \tag{15}$$

Here, f_{rout} must be inserted in Hz. The other terms are the output amplifier responsivity OAR and the detector off-chip noise off_n. The numerical values of such quantities can be found in Table 4.

Quantization noise. The QN is computed with the following equation (Cipriano et al., 2018)

$$\sigma_{QN} = \frac{0.7 \; C_i}{2^{N_{bits}} \; \sqrt{12}} \tag{16}$$

where C_i is the detector pixel capacity, which is equal to the charge handling capacity C when the gain capability of the CCD is not exploited. Differently, it is equal to the charge handling capacity of the multiplication register C_{MR} when the signal is amplified with gain $G \neq 1$. The term N_{bits} is the bit number of the A/D converter, equal to 14 in the specific case of the LUMIO-Cam.

Straylight noise. A straylight analysis has been carried out to understand the impact of the Sun residual image onto the observed scene. Five cases of baffle length (from 0 up to 200 mm) have been investigated. Eventually, a baffle length of 150 mm has been selected as a result of a configuration trade-off and used to perform the radiometric analysis to assess LUMIO-Cam performance.

To carry out the straylight analysis, the following assumptions have been made: the baffle and the mechanical structure that supports the
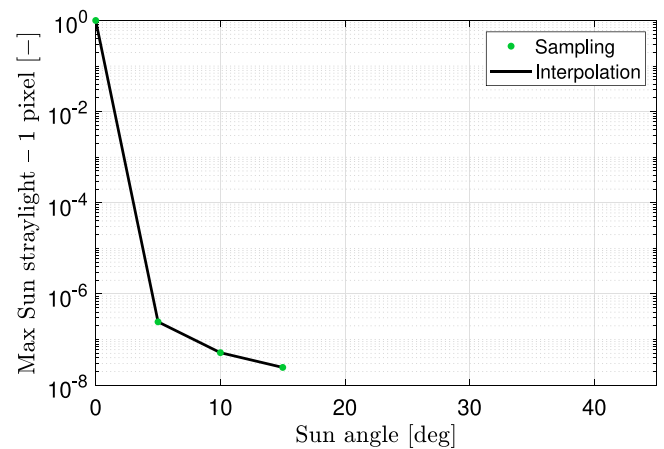

Fig. 11. Maximum normalized Sun straylight on one pixel due to ghosts as a function of the Sun angle. Linear interpolation. Semi-log scale plot.

lenses are considered perfectly absorbent, the coated optical surfaces are assumed to have a residual reflectivity equal to 1%, the focal plane assembly (FPA) surface is assumed to have a residual reflectivity equal to 20%, the contamination level of the external optical surface is assumed equal to 800 ppm, the contamination level of the internal optical surfaces is 100 ppm, and the roughness of the optical surfaces is modeled with the standard FRED Optical Engineering Software (FRED) polished surface scatter model.

In the analysis, the following sources of residual images of the out-of-field Sun have been considered: ghost images given by double residual reflections on optical surfaces, scattering due to contamination on optical surfaces (e.g., dust), and scattering due to residual roughness of optical surfaces after polishing. Generally speaking, ghost images depend on the wavelength through the residual reflectivity wavelength dependence. However, they are wavelength-independent in the simplified model employed. On the other hand, the scattering from contamination and roughness of the optical surfaces depends on the wavelength. Therefore, two analysis at 400 nm and 900 nm have been performed.

The estimated maxima of Sun straylight collected on a single pixel considering the Sun as an extended source in the case of a 150 mm baffle length are presented in Table 5. The Sun signal on one pixel due to ghosts as a function of the Sun angle is shown in Fig. 11. Then, the Sun signal on one pixel due to contamination as a function of the Sun angle and the wavelength is shown in Fig. 12. Finally, the Sun signal on one pixel due to roughness as a function of the Sun angle and the wavelength is shown in Fig. 13.

To compute the Sun straylight signal due to ghosts the following formula has been used

$$s_{sl,\odot,ghosts} = \frac{A_{oa}}{A_{d,\odot S/C}} A_{GSD} \Delta t_{exp} f_{sl,ghosts} \left(\theta_\odot \right) \int_{\lambda_1}^{\lambda_2} N_{e^-}(\lambda, T_\odot) d\lambda \tag{17}$$

where $A_{oa,\perp} = \pi D^2 \cos(\theta)/4$ is the surface of optics aperture, $A_{d,\odot S/C} = 2\pi d_{\odot S/C}^2$ is the scaling factor to compute the flux at observer distance,[19] d is the distance from LUMIO to the Sun, A_{GSD} is the area of the Sun surface corresponding to the IFOV at distance $d_{\odot S/C}$, and $f_{sl,ghosts} \left(\theta_\odot \right)$ is the maximum normalized Sun straylight on one pixel due to ghosts as a function of the Sun angle and $\theta_\odot$ is the Sun angle considered. Then, Δt_{exp} is the integration time of the camera and $T_\odot = 5800\,K$ is the assumed Sun surface temperature used to get the spectral emissive power. The integration domain depends on the LUMIO-Cam channel.

Table 5
Sun signal on one pixel normalized to direct Sun signal. Coefficients for baffle length 150 mm.

Sun angle	Ghosts	Contamination		Roughness	
		400 nm	900 nm	400 nm	900 nm
[deg]	[−][a]	[−]	[−]	[−]	[−]
0	1	1	1	1	1
5	2.45×10^{-7}	7.34×10^{-8}	6.30×10^{-8}	1.94×10^{-7}	2.55×10^{-7}
10	5.16×10^{-8}	2.32×10^{-8}	2.34×10^{-8}	7.30×10^{-8}	8.02×10^{-8}
15	2.45×10^{-8}	2.32×10^{-8}	1.94×10^{-8}	4.85×10^{-8}	4.81×10^{-8}
20	0	0	0	0	2.35×10^{-8}
25	0	0	0	0	0

[a]Throughout the work, the symbol [−] indicates a dimensionless quantity.
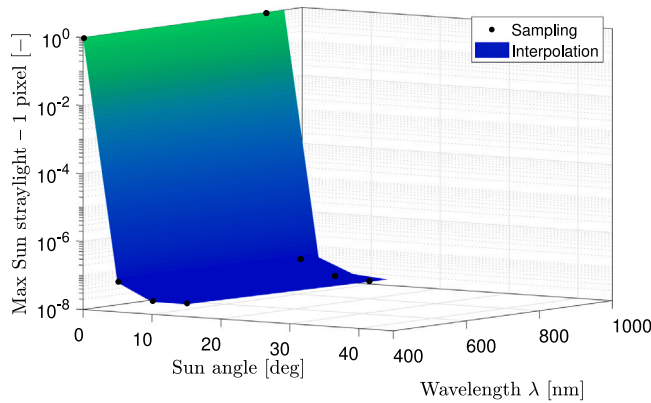

Fig. 12. Maximum normalized Sun straylight on one pixel due to contamination as a function of the Sun angle and the wavelength. Bilinear interpolation. Semi-log scale plot.
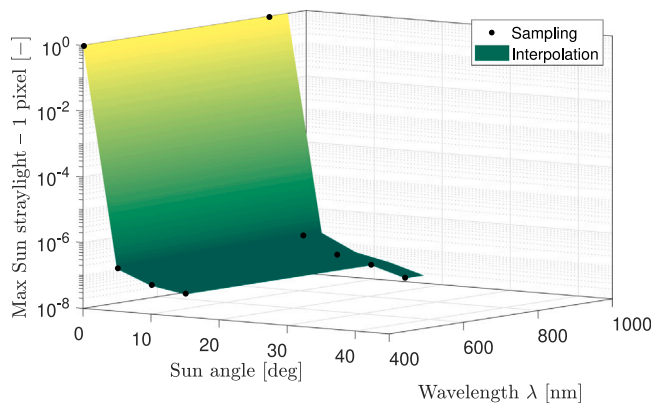

Fig. 13. Maximum normalized Sun straylight on one pixel due to roughness as a function of the Sun angle and the wavelength. Bilinear interpolation. Semi-log scale plot.

To compute the Sun straylight signal due to contamination the following formula has been used

$$s_{\mathrm{sl},\odot,\mathrm{cont}} = \frac{A_{\mathrm{oa}}}{A_{d,\odot \mathrm{S/C}}} A_{\mathrm{GSD}} \Delta t_{\exp} \int_{\lambda_1}^{\lambda_2} N_{e^-}(\lambda, T_\odot) f_{\mathrm{sl,cont}}(\theta_\odot, \lambda)\, \mathrm{d}\lambda \quad (18)$$

where $f_{\mathrm{sl,cont}}(\theta_\odot, \lambda)$ is the maximum normalized Sun straylight on one pixel due to contamination as a function of the Sun angle and the wavelength.

To compute the Sun straylight signal due to roughness the following formula has been used

$$s_{\mathrm{sl},\odot,\mathrm{rough}} = \frac{A_{\mathrm{oa}}}{A_{d,\odot \mathrm{S/C}}} A_{\mathrm{GSD}} \Delta t_{\exp} \int_{\lambda_1}^{\lambda_2} N_{e^-}(\lambda, T_\odot) f_{\mathrm{sl,rough}}(\theta_\odot, \lambda)\, \mathrm{d}\lambda \quad (19)$$

where $f_{\mathrm{sl,rough}}(\theta_\odot, \lambda)$ is the maximum normalized Sun straylight on one pixel due to contamination, which depends on the Sun angle and the wavelength.

Finally, the total straylight signal due to the Sun is computed as

$$s_{\mathrm{sl},\odot} = s_{\mathrm{sl},\odot,\mathrm{ghosts}} + s_{\mathrm{sl},\odot,\mathrm{cont}} + s_{\mathrm{sl},\odot,\mathrm{rough}} \quad (20)$$

while its Poisson noise is $\sigma_{\mathrm{sl},\odot} = \sqrt{s_{\mathrm{sl},\odot}}$.

Additionally, the straylight coming from the illuminated side of the Moon, the albedo, should be considered as an additional source of noise. The Moon is always in the field of view during observation because of the continuous pointing of the LUMIO-Cam towards its center. Consequently, the pixels affected by the straylight coming from the illuminated side of the Moon are only those looking at the terminator line. However, to be conservative, the pixel is assumed to collect some of that straylight, independently on the impact location. To account for that contribution the Moon is put slightly out of the LUMIO-Cam field of view, at $\bar{\theta}_{\mathbb{C}} = 5$ deg. The second row of Table 5 is used to evaluate the albedo straylight contribution.

To compute the Moon albedo straylight signal due to ghosts the following formula has been used

$$s_{\mathrm{sl},\mathbb{C},\mathrm{ghosts}} = \frac{A_\odot A_{\mathrm{GSD}} A_{\mathrm{oa}}}{A_{d,\odot \mathbb{C}} A_{d,\odot \mathrm{S/C}}} \Delta t_{\exp} f_{\mathrm{sl,ghosts}}(\bar{\theta}_{\mathbb{C}}) f_{\mathrm{illu}}(\theta_\odot)$$
$$\times \int_{\lambda_1}^{\lambda_2} N_{e^-}(\lambda, T_\odot) \varepsilon_{\mathbb{C}}\, \mathrm{d}\lambda \quad (21)$$

where the temperature of the Sun $T_\odot = 5800$ K is used to get the spectral emissive power. The power is firstly multiplied by the Sun surface area $A_\odot = 4\pi R_\odot^2$, then scaled by the Sun–Moon distance $d_{\odot \mathbb{C}}$ through the term $A_{d,\odot \mathbb{C}} = 4\pi d_{\odot \mathbb{C}}^2$. To get the power reflected by the Moon, it is used the lunar mean albedo $\varepsilon_{\mathbb{C}} = 0.11$ and the flux is multiplied by the IFOV area A_{GSD}. A_{GSD} is computed in the planar approximation according to Eq. (10). Scaling with respect to LUMIO distance is done through $A_{d,\odot \mathrm{S/C}} = 2\pi h^2$, where h is the CubeSat range. $f_{\mathrm{sl,ghosts}}(\bar{\theta}_{\mathbb{C}})$ is the maximum normalized Sun straylight on one pixel due to ghosts evaluated at $\bar{\theta}_{\mathbb{C}} = 5$ deg. The extremes of integration depend on the LUMIO-Cam channel considered. Since the illuminated fraction of the Moon (and so the straylight) varies as a function of the position of the Sun, the term $f_{\mathrm{illu}}(\theta_\odot)$ is used as an approximation to scale the straylight linearly with the Sun angle

$$f_{\mathrm{illu}}(\theta_\odot) = \frac{\theta_\odot}{180} \quad (22)$$

where $\theta_\odot$ is in deg.

To compute the Moon albedo straylight signal due to contamination the following formula has been used

$$s_{\mathrm{sl},\mathbb{C},\mathrm{cont}} = \frac{A_\odot A_{\mathrm{GSD}} A_{\mathrm{oa}}}{A_{d,\odot \mathbb{C}} A_{d,\odot \mathrm{S/C}}} \Delta t_{\exp} f_{\mathrm{illu}}(\theta_\odot)$$
$$\times \int_{\lambda_1}^{\lambda_2} N_{e^-}(\lambda, T_\odot) f_{\mathrm{sl,cont}}(\bar{\theta}_{\mathbb{C}}, \lambda) \varepsilon_{\mathbb{C}}\, \mathrm{d}\lambda \quad (23)$$

where $f_{\mathrm{sl,cont}}(\bar{\theta}_{\mathbb{C}}, \lambda)$ is the maximum normalized Sun straylight on one pixel due to contamination depending on the wavelength and evaluated at $\bar{\theta}_{\mathbb{C}} = 5$ deg.

The Moon albedo straylight signal due to roughness is computed as

$$
s_{\text{sl},\mathbb{C},\text{rough}} = \frac{A_{\odot} A_{\text{GSD}} A_{\text{oa}}}{A_{d,\odot\mathbb{C}} A_{d,\odot\text{S/C}}} \Delta t_{\text{exp}} f_{\text{illu}}\left(\theta_{\odot}\right)
$$
$$
\times \int_{\lambda_1}^{\lambda_2} N_{e^-}(\lambda, T_{\odot}) f_{\text{sl,rough}}\left(\bar{\theta}_{\mathbb{C}}, \lambda\right) \varepsilon_{\mathbb{C}} \, \mathrm{d}\lambda \tag{24}
$$

where $f_{\text{sl,rough}}\left(\bar{\theta}_{\mathbb{C}}, \lambda\right)$ is the maximum normalized Sun straylight on one pixel due to roughness evaluated at $\bar{\theta}_{\mathbb{C}} = 5\,\text{deg}$.

In the end, the total straylight signal due to the Moon albedo is computed as

$$
s_{\text{sl},\mathbb{C}} = s_{\text{sl},\mathbb{C},\text{ghosts}} + s_{\text{sl},\mathbb{C},\text{cont}} + s_{\text{sl},\mathbb{C},\text{rough}} \tag{25}
$$

while the corresponding Poisson noise is $\sigma_{\text{sl},\mathbb{C}} = \sqrt{s_{\text{sl},\mathbb{C}}}$.

The overall straylight signal is computed as $s_{\text{sl}} = s_{\text{sl},\mathbb{C}} + s_{\text{sl},\odot}$. The corresponding associated Poisson noise being $\sigma_{\text{sl}} = \sqrt{s_{\text{sl}}}$.

4.3. SNR computation

The detectors mounted in the two channels allow to amplify the signals generated in the pixels before the multiplication register by a factor G. They are s_{imp}, $s_{\mathbb{C}}$, σ_{sl}, and s_{DC}. The signal amplification increases also the total Poisson noise. That is accounted by means of the excess noise factor (ENF) F. The expression to evaluate the SNR in dB is

$$
\text{SNR} = 10 \log_{10}\left(\frac{G s_{\text{imp}}}{\sqrt{F^2 \, G\left(\sigma_{\text{imp}}^2 + \sigma_{\mathbb{C}}^2 + \sigma_{\text{sl}}^2 + \sigma_{\text{DC}}^2\right) + \sigma_{\text{RON}}^2 + \sigma_{\text{OCN}}^2 + \sigma_{\text{QN}}^2}}\right). \tag{26}
$$

If the signal is not amplified ($G = 1$) the ENF is put equal to 1. The numerical value of the ENF is $F = \sqrt{2}$ (see Table 4). The term σ_{sl} is set to 0 when the straylight noise is neglected.

The signal is cut at wavelength λ_{dic} because of the dichroic lens. Consequently, the two channels receive signals in different bandwidths. When solving the finite integrals to compute the SNR for VIS channel the integration extremes are $\lambda_1 = 450\,\text{nm}$ (lower bound of LUMIO-Cam sensitivity range, see Table 4) and $\lambda_2 = \lambda_{\text{dic}}$. On the other hand, when considering the NIR channel the extremes of integration are $\lambda_1 = \lambda_{\text{dic}}$ and $\lambda_2 = 950\,\text{nm}$ (upper bound of LUMIO-Cam sensitivity range, see Table 4).

5. Radiometric analysis

In the radiometric analysis, the required minimum SNR has been set to 10 dB, to be conservative. The saturation has been set to occur when more than half of the impacts at a given kinetic energy saturate the detector. In the first part of the radiometric analysis straylight has been neglected. A dedicated analysis accounting for straylight noise has been performed separately and its results are discussed in Section 5.1.

DC noise, RON, OCN, and QN depend only on the LUMIO-Cam specifics and have the same values for both channels. They are collected in Table 6. On the contrary, the Moon surface background noise is different for the two channels (see Table 7). Depending on the Sun angle, only one between the Sun straylight noise and the Moon albedo straylight noise affects the observations. Indeed, as shown in Fig. 14, for small Sun angles the Sun contribution is predominant, while for Sun angles larger than 20 deg it is the Moon albedo that affects the measurements.

The first set of results performed in the radiometric analysis is about how the SNR varies with respect to the impact kinetic energy of the meteoroid. The charts in Fig. 15 show the different behavior of the two channels at different distances of LUMIO from the Moon and for the three significant case studies of signal peak location. The

Table 6
LUMIO-Cam internal Poisson noises.

Source	Poisson noise [e⁻ rms]
σ_{DC}	3.31
σ_{RON}	7.06
σ_{OCN}	1.01×10^2
σ_{QN}	9.00

Table 7
Poisson noise of the Moon background.

	Channel:	VIS	NIR
$\sigma_{\mathbb{C}}$ [a]	[e⁻ rms]	7.60×10^{-18}	1.21×10^{-14}

[a] Computations performed in the planar approximation and with the impact occurring at nadir.
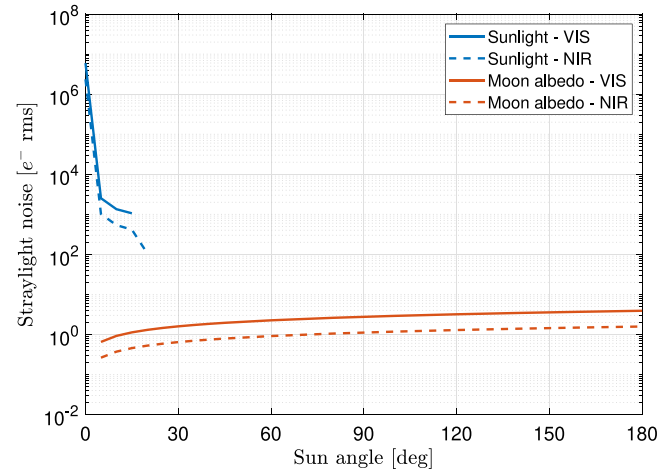

Fig. 14. Straylight noise as a function of the Sun angle in one pixel. The blue curves are the contributions of the Sun, while the red ones are the contribution of the Moon albedo. The solid curves show the straylight noise affecting the VIS channel, while the dashed ones show the straylight noise affecting the NIR channel. Semi-log scale plot.

impact energies that saturate the detector are highlighted in yellow. The charts have been plotted fixing the LUMIO-Cam gain G at 10. The curves have been computed simulating 1000 impacts for several impact kinetic energy values. The impact velocity is drawn from a truncated Gaussian distribution (see Section 4.1) for each individual impact. The mass of the particle is derived accordingly. The size, the flash duration, the equivalent black body temperature of the plume, and the other quantities required to perform the radiometric analysis are modeled according to the methodology described in Merisio and Topputo (2022). Clearly, the range of impact kinetic energies which can be detected depends strongly on the distance from the Moon and on the spread fraction of the impact flash on the pixel. The most common case should be the one in which the spread fraction is $1/2$.

Keeping the gain fixed does not allow to cover properly the whole range of impact kinetic energies of interest. In particular, the more energetic impacts saturate the detectors of the two channels frequently. On the other hand, results suggest that the less energetic impacts are properly detected. Remarkably, over the 99% of the registered impacts do not saturate the detectors and are successfully detected[20] by the LUMIO-Cam. In fact, meteoroids are distributed according to a power

---

[20] With successfully detected we intend those impact flashes whose measurements allow inferring the projectile impact kinetic energy and the flash temperature (if detection by both VIS and NIR channels is confirmed). Conversely, for flashes saturating the CCD detectors only a lower bound on the impact kinetic energy can be inferred from their measurements.
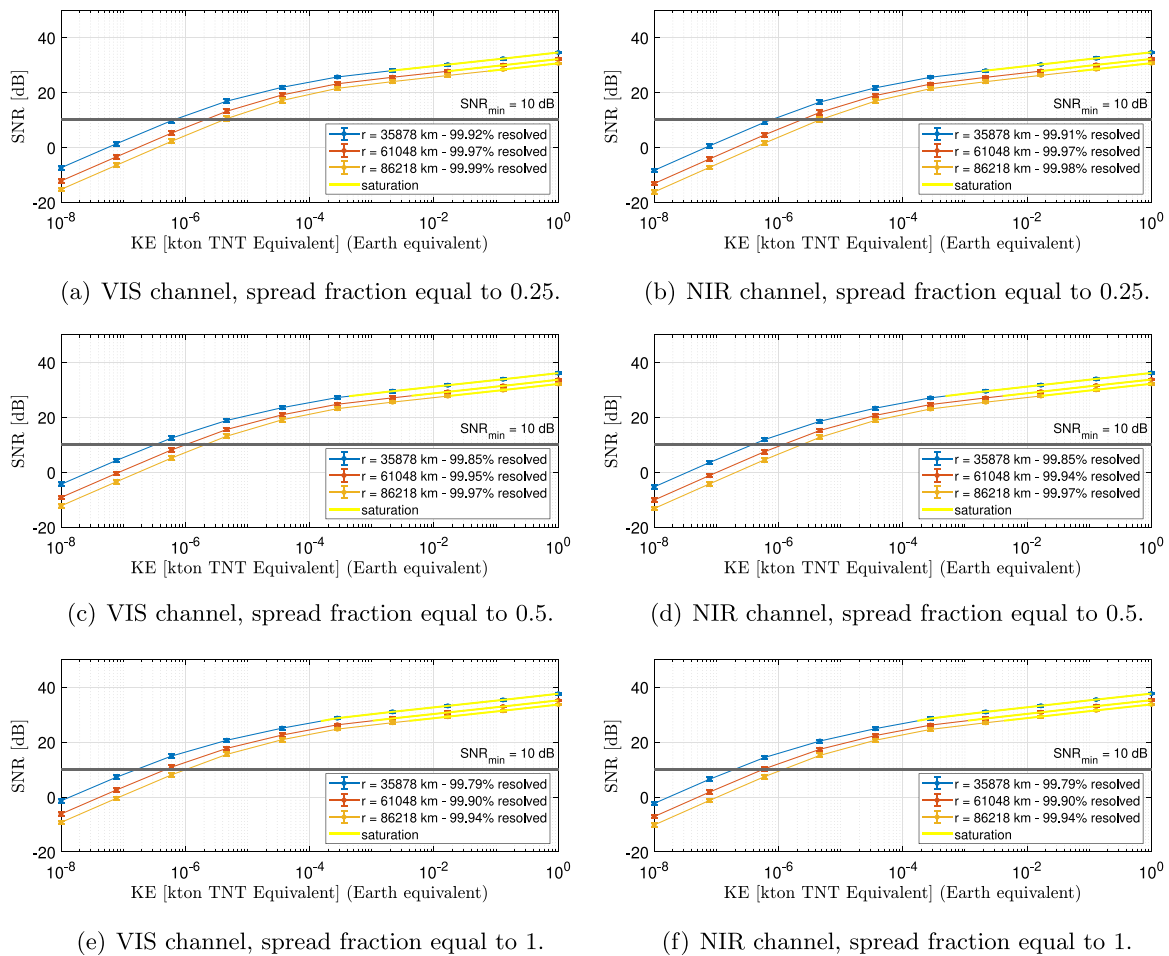
(a) VIS channel, spread fraction equal to 0.25.

(b) NIR channel, spread fraction equal to 0.25.

(c) VIS channel, spread fraction equal to 0.5.

(d) NIR channel, spread fraction equal to 0.5.

(e) VIS channel, spread fraction equal to 1.

(f) NIR channel, spread fraction equal to 1.

Fig. 15. Radiometric analysis about impact flash detection (straylight not included). The SNR as a function of the impact kinetic energy in Earth equivalent is drawn for significant cases. The plots show how the SNR varies in the two channels for the three different cases of flash impact peak location within the central pixel of the detector. In each chart the SNR for different distances from the Moon of LUMIO is plotted. In yellow are identified the impact kinetic energies that saturate the detectors. The black horizontal line marks the conservative threshold of minimum SNR of 10 dB. The legends contain information about the percentage of detected impacts that do not saturate the LUMIO-Cam. Gain G fixed at 10. For each given impact kinetic energy, 1000 impacts have been simulated. Semi-log scale plots.

law with respect to the impact kinetic energy (Brown et al., 2002; Suggs et al., 2014).

The plots in Fig. 16 present an investigation about the value of the LUMIO-Cam gain G required to resolve an impact at the minimum SNR for different distances of LUMIO and impact kinetic energies of the meteoroids. Results for both channels are shown. The cases in which the detectors saturate are highlighted in yellow. The case with spread fraction equal to 1/2 has been considered. The gain can assume values only within the range $[1, 1000]$. Plots show clearly how high energy impacts saturate the detectors when LUMIO is closer to the Moon.

In Fig. 17, the investigation about the detectability range of impact kinetic energies for VIS and NIR is shown. The first set of curves, marked with full circles, shows how the distance at which the minimum SNR is granted varies with respect to the impact kinetic energy in Earth equivalent given a value of the camera gain. On the other hand, the second set of curves, marked with full triangles, shows the distances at which the detectors saturate as a function of the impact kinetic energy and fixing the camera gain. To draw the curves, the case with spread fraction equal to 1/2 has been considered.

The charts in Fig. 17 can be used to properly select the gains for the channels depending on the distance of LUMIO from the Moon. Indeed, the set of impact kinetic energies between the two curves represents the detectability range at the distance and for the specific gain characteristic of those curves. Therefore, given a distance, the gain that maximizes the detectability range can be selected by visual inspection. Differently,

one can select the gain to customize the detectability range at a certain distance in order to satisfy specific requirements of the mission.

The curves describing the saturation condition when the gain is 1 and 10 are very close because of two different kinds of saturation that may occur in the detectors. The first occurs when the pixel saturates (charge handling capacity C in Table 4), while the second happens when the multiplication register saturates (charge handling capacity of the multiplication register C_{MR} in Table 4). In the case of $G = 1$, the pixel reaches its maximum capacity before the multiplication register, potentially causing a definitely undesired bleeding effect. On the other hand, when $G \geq 10$, the multiplication register reaches its maximum capacity first. Results suggest that selecting $G = 10$ avoids insurgence of bleeding and increases the detectability range. Specifically, at larger distances, part of the more energetic impacts could be detected without losing performance at lower impact kinetic energies. The selected values of the gains for VIS and NIR channels are presented in Fig. 18. The chart shows the selected gains at different LUMIO–Moon distances.

5.1. Results accounting for the straylight noise

Results of the radiometric analysis accounting for the straylight are herewith presented. Observation cannot be performed for Sun angles smaller than 20 deg due to the large Sun straylight contribution affecting measurements (Table 5 and Fig. 14). However, for Sun angles larger than 20 deg, the Sun straylight contribution is completely
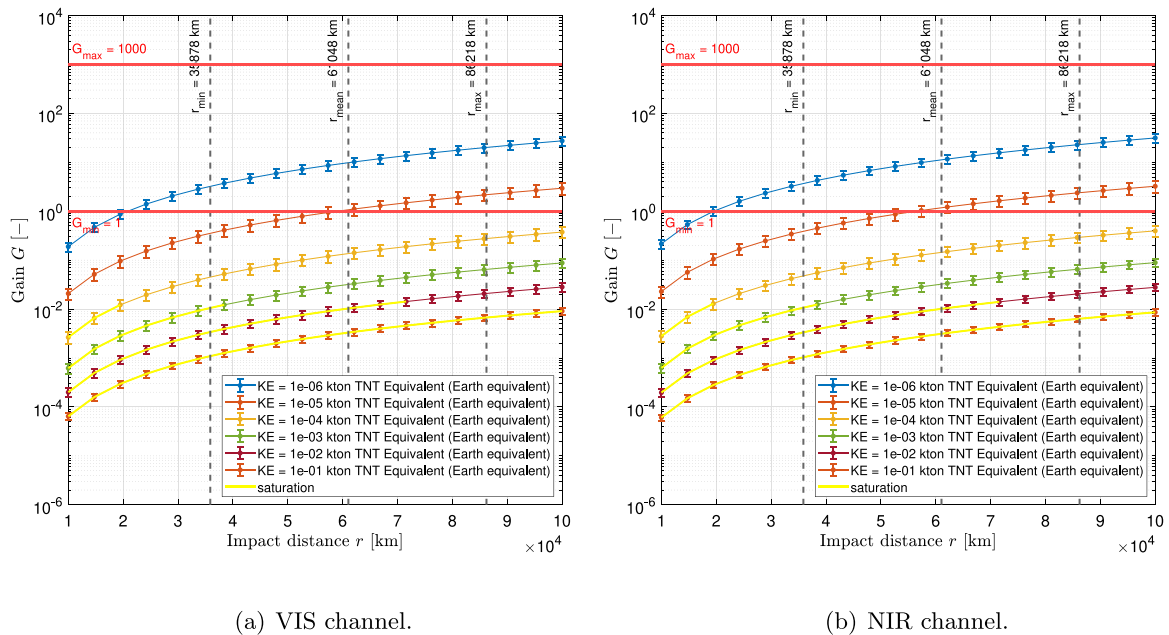
(a) VIS channel.

(b) NIR channel.

Fig. 16. Investigation about the gain of the LUMIO-Cam. Gain required to satisfy the minimum SNR condition (10 dB) as a function of the distance of LUMIO from the center of the Moon. The plots show how the curves change for the two channels and for different values of the impact kinetic energy in Earth equivalent. In yellow are identified the distances at which the detector saturates. The red horizontal lines mark the feasibility domain for the LUMIO-Cam gain. The black dashed vertical lines mark significant distances of LUMIO during the operative phase of the mission. Spread fraction equal to 1/2. For each given distance, 1000 impacts have been simulated. Semi-log scale plots.

suppressed. Therefore, only the Moon albedo contribution can affect measurements.

Two significant cases are considered here. The first is when the Sun angle is equal to 20 deg and the second when the Sun angle is 90 deg. The latter corresponds to the 50% illumination of the Moon. For greater Sun angles the scientific observation is not performed according to the concept of operations (see Fig. 3). Consequently, from Fig. 14, the worst case scenario is when the Sun angle is equal to 90 deg.

Results for Sun angle equal to 20 deg are shown in Fig. 19, while Fig. 20 shows the results when the Sun angle is 90 deg. Comparing plots in Figs. 19–20 with the charts in Fig. 15, it seems that the straylight noise due to the Moon albedo does not degrade measurements when a 150 mm baffle is used and the Sun angle is between 20 deg and 90 deg. Equipping the LUMIO-Cam with a 150 mm baffle should be enough to grant good performance in terms of impact flashes SNR.

6. POE integrated analysis

Results of the integrated analysis follow. A Monte Carlo analysis has been carried out to estimate the scientific return of LUMIO considering the operational quasi-halo orbit, the payload, and the meteoroid environment.

The methodology consists in the following steps: (i) supply of inputs (operational orbit states in the form of a Spacecraft Planet Instrument Camera–matrix Events (SPICE) ephemeris kernel (Acton, 1996; Acton et al., 2018), LUMIO-Cam specifics, minimum impact kinetic energy, and time span); (ii) generation of all SPICE kernels related to CubeSat attitude and optical instrument geometry; (iii) generation of the sample meteoroid environment scenario according to Merisio and Topputo (2022); (iv) evaluation of the SNR of a subset of meteoroids; (v) estimation of the number of detections; (vi) computation of the performance parameters. To carry out a Monte Carlo analysis steps (iii), (iv), and (v) can be repeated N times. Fig. 21 shows a schematic representation of the coverage analysis methodology.

The estimation of the scientific return of the LUMIO lunar CubeSat is derived in terms of a set of statistical performance parameters. They are the number of detected impact flashes $\mathcal{N}_{det}$, the number of

impact flashes that saturate the CCD $\mathcal{N}_{sat}$, the number of detected impact flashes with impact kinetic energy in the range at Earth from 10^{-4} to 10^{-1} kton TNT Equivalent $\mathcal{N}_{high}$, the number of detected impact flashes with impact kinetic energy in the range at Earth from 10^{-6} to 10^{-4} kton TNT Equivalent $\mathcal{N}_{low}$, the minimum impact kinetic energy associated to a detected impact flash $KE_{det,min}$, the maximum impact kinetic energy associated to a detected impact flash $KE_{det,max}$, the minimum meteoroid mass associated to a detected impact flash $m_{det,min}$, the maximum meteoroid mass associated to a detected impact flash $m_{det,max}$, the number of detected impact flashes belonging to a source $\mathcal{N}_{det,AAA}$ where the subscript AAA represents the IAU code (Jenniskens et al., 2009), and the temporal distribution of detected impact flashes. $KE_{det,max}$ and $m_{det,max}$ are computed from the subsets of impact flashes that are detected. Indeed, for flashes that saturate the CCD, only a lower limit on the impact kinetic energy can be estimated in practice.

The setup of the meteoroid environment model used for the Monte Carlo analysis is reported in Table 8. The operational orbit considered is the quasi-halo about Earth–Moon L_2 Lagrangian point with Jacobi's constant $C_j = 3.09$ (Cipriano et al., 2018). The sequence of science and navigation & engineering cycles proposed as concept of operations has been taken into account. The LUMIO-Cam specifics supplied as inputs are collected in Table 4.

The performance parameters of the integrated analysis are collected in Table 9. Overall, more than 10 000 detections are expected. The majority of them belong to the equivalent impact kinetic energy range at the Earth from 10^{-6} to 10^{-4} kton TNT Equivalent. The high number of detected flashes estimated may be justified by the following considerations.

One of the first estimations reported in the literature about a monitoring mission of lunar impacts is found in Koschny and McAuliffe (2009). It reports a rough estimation of one to several impacts per hour of observation, depending on the mission characteristics. To derive that estimate, the impact rate provided in Grün et al. (1985) has been used. Assuming 1 observation per hour, for a mission with an operational lifetime of 1 year that continuously monitors the Moon for half of the year (accounting for the illumination cycle of the Moon) the number of observations is roughly 4392 (24 meteoroids detected times 183
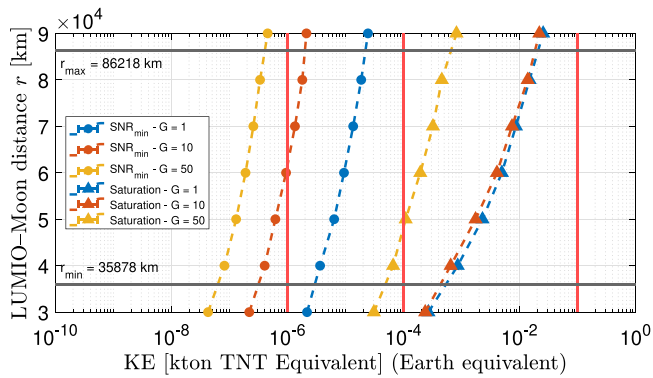
(a) VIS channel.
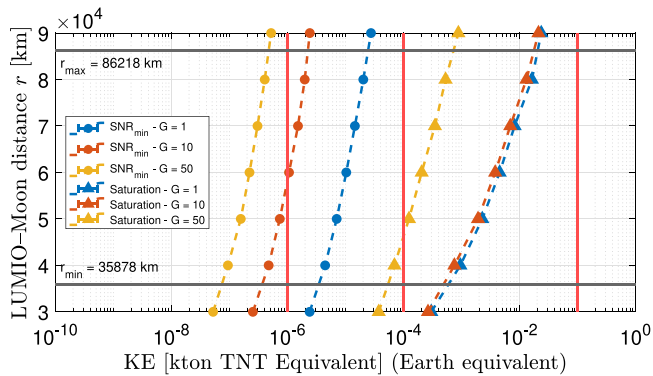
(b) NIR channel.

Fig. 17. Detected range of impact kinetic energies. The first set of curves, marked by full circles, shows the distance of LUMIO from the center of the Moon in order to achieve the minimum SNR (10 dB) as a function of the impact kinetic energy in Earth equivalent. The second set of curves, marked by full triangles, shows the minimum distance at which the detector saturates as a function of the impact kinetic energy in Earth equivalent. The plots are drawn for both channels and for different values of the LUMIO-Cam gain. The red vertical lines mark the impact kinetic energies of interest for the mission. The black horizontal lines mark the minimum and maximum distances of LUMIO during the operative phase of the mission. Spread fraction equal to 1/2. Given a distance and a gain, the set of impact kinetic energies between the two curves is the detectability range. The gain can be properly selected in order to maximize the detectability range at every distance. Semi-log scale plots.
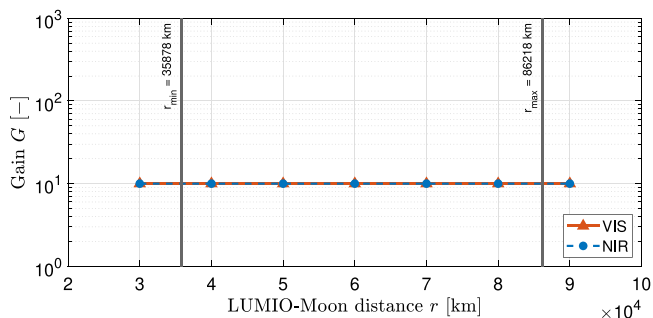

Fig. 18. Selected gains of VIS, red triangles, and NIR, blue circles, as a function of the distance of LUMIO from the center of the Moon. The black horizontal lines mark the minimum and maximum distances of LUMIO during the operative phase of the mission. Semi-log scale plot.

days). The estimation is one order of magnitude smaller than the one presented in Table 9. However, in Koschny and McAuliffe (2009), it is assumed that the number of impacts which are effectively detectable is approximately 50% of the total due to shadowing effects of lunar mountains. Differently, an obstruction of 20% is assumed in Merisio

Table 8
Inputs to carry out the integrated Monte Carlo analysis.

Setup		Value
Target	–	Moon
Time window beginning	t_i	21 March 2024 12:00:00.0 UTC
Time window ending	t_f	21 March 2025 12:00:00.0 UTC
Time step	Δt	1 h
Min kinetic energy at the Moon	$KE_{\mathbb{C},min}$	4.88×10^{-7} kton TNT Equivalent
Min kinetic energy at the Earth	$KE_{\oplus,min}$	10^{-6} kton TNT Equivalent
Random scenarios	N_{scn}	10^3

Table 9
Scientific return of the LUMIO lunar CubeSat mission.

Performance parameter		Mean	Standard deviation
$\mathcal{N}_{det}$	[#]	3.7×10^4	8.3×10^2
$\mathcal{N}_{sat}$	[#]	9.2×10^1	9.5
$\mathcal{N}_{det,high}$	[#]	7.2×10^2	2.8×10^1
$\mathcal{N}_{det,low}$	[#]	3.6×10^4	8.2×10^2
$KE_{det,min}$	[kton TNT Equivalent]	7.3×10^{-7}	2.6×10^{-11}
$KE_{det,max}$	[kton TNT Equivalent]	5.3×10^{-3}	2.7×10^{-3}
$m_{det,min}$	[kg]	1.2×10^{-3}	1.7×10^{-5}
$m_{det,max}$	[kg]	1.3×10^2	1.3×10^2

and Topputo (2022) because of the larger distances of LUMIO from the Moon with respect to the low-orbiting lunar satellite discussed in Koschny and McAuliffe (2009). The latter assumption rises the estimation of observed flashes considerably.

A more recent estimation is the one of the Phase 0 study used in the operational orbit trade-off (Cipriano et al., 2018). During Phase 0, the analysis has been carried out exploiting two different methodologies named the luminous efficiency method and the black body method. For the selected operative orbit and a 1 year mission operational lifetime the luminous efficiency method predicts ≈4200 detections while the black body method ≈5500 (Cipriano et al., 2018). Both estimations refer to the number of impact flashes successfully detected. They have been derived scaling to the Moon the terrestrial impact rate in Brown et al. (2002).

However, for impact kinetic energies close to the minimum value detected, the impact frequency according to Merisio and Topputo (2022) is closer to the impact rate proposed in Ortiz et al. (2015) than to that in Brown et al. (2002). The yearly number of meteoroids impacting the total lunar surface with energy greater than or equal to 5×10^{-7} kton TNT Equivalent is estimated to be 31 229 according to the power law in Brown et al. (2002) and 427 400 according to the more recent one in Ortiz et al. (2015). The impact kinetic energy used for the computations is slightly larger than the minimum kinetic energy detectable by LUMIO estimated both in this study and in Cipriano et al. (2018), therefore it is likely that less impacts are counted. Considering an observational period of half-year, an obstruction coefficient of 20%, and an observed surface corresponding to the 3/8 of the whole lunar surface,[21] an over-estimation of detected flashes is roughly 4684 and 64 110 according to the power laws in Brown et al. (2002) and Ortiz et al. (2015), respectively.

The number of impacts obtained using the power law from Ortiz et al. (2015) is about 13.7 times larger than that predicted employing the power law from Brown et al. (2002). It is reasonable to expect

---

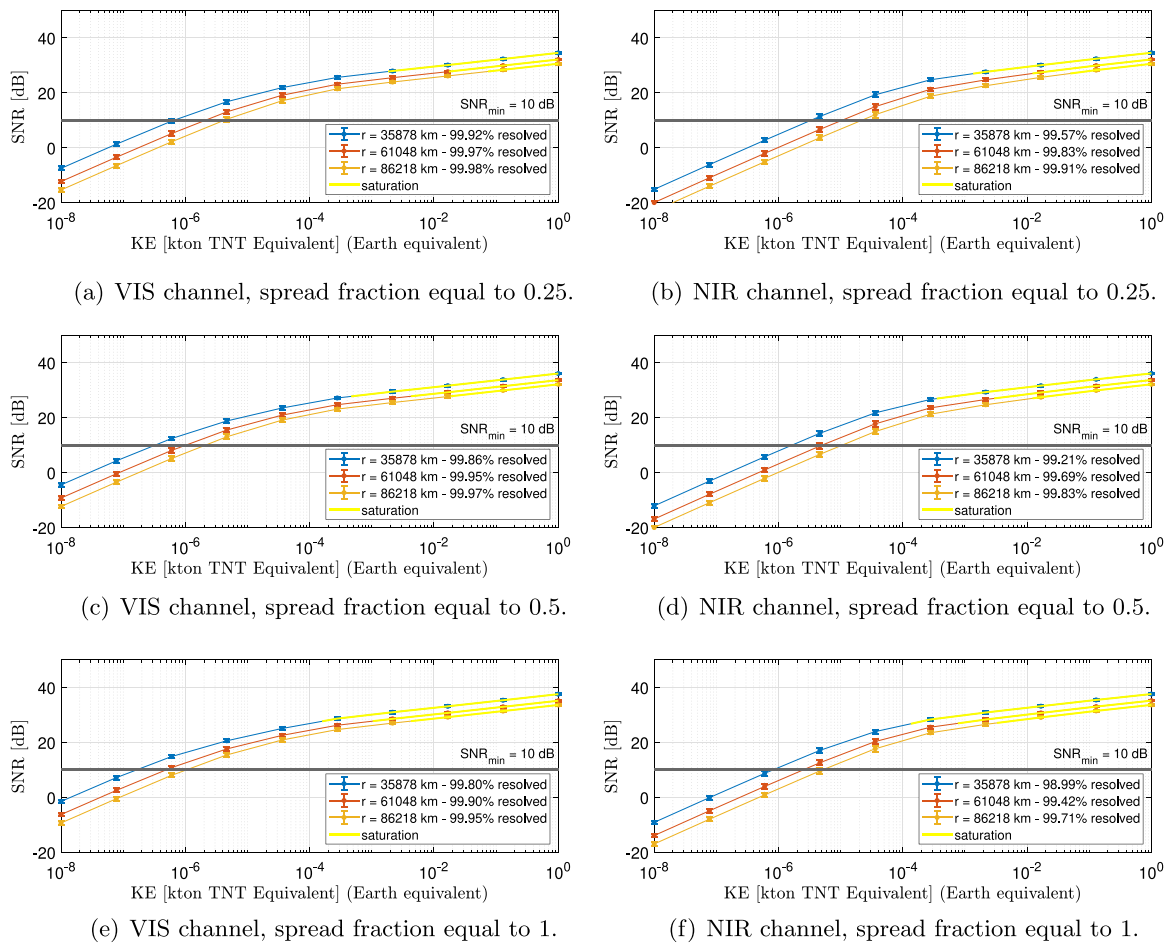[21] Roughly the average lunar dark surface observed by LUMIO during its operational lifetime.

(a) VIS channel, spread fraction equal to 0.25.

(b) NIR channel, spread fraction equal to 0.25.

(c) VIS channel, spread fraction equal to 0.5.

(d) NIR channel, spread fraction equal to 0.5.

(e) VIS channel, spread fraction equal to 1.

(f) NIR channel, spread fraction equal to 1.

Fig. 19. Radiometric analysis about impact flash detection accounting for straylight, Sun angle equal to $20\,\mathrm{deg}$. The SNR as a function of the impact kinetic energy in Earth equivalent is drawn for significant cases. The plots show how the SNR varies in the two channels for the three different cases of flash impact peak location within the central pixel of the detector. In each chart the SNR for different distances from the Moon of LUMIO is plotted. In yellow are identified the impact kinetic energies that saturate the detectors. The black horizontal line marks the conservative threshold of minimum SNR of $10\,\mathrm{dB}$. The legends contain information about the percentage of detected impacts that do not saturate the LUMIO-Cam. Gain G fixed at 10. For each given impact kinetic energy, 1000 impacts have been simulated. Semi-log scale plots.

that also the number of detected flashes could rise of approximately the same factor if using a modeling of the meteoroid environment which foresees a flux similar to the one presented in Ortiz et al. (2015). Moreover, in the range about 10^{-7} kton TNT Equivalent, the meteoroid flux proposed in Grün et al. (1985) gives a rate which is similar to that returned by the power law in Brown et al. (2002). Thus, the considerations about the estimates in Cipriano et al. (2018) apply also to the ones reported in Koschny and McAuliffe (2009). The previous remarks may justify the large number of observed flashes estimated through the integrated POE methodology. The number of estimated observations depends strongly on the meteoroid flux power law used in the modeling of the meteoroid environment.

The temporal distribution of the detected lunar impact flashes is shown on the left y-axis of Fig. 22. It is represented by the red dots connected with the dotted red line. The cumulative temporal distribution is shown on the left y-axis of Fig. 23, identified by the red dots connected with the dotted red line. In both plots, dots identify average values, while error bars represent the standard deviations from the means. The phase angle β is drawn on the background of both charts. The gray shaded areas highlight the time windows in which monitoring is unfeasible because of the high Moon illumination. The gray areas are consistent with the concept of operations of the mission (see Fig. 3). Differently, the orange shaded areas feature the epochs in which the Sun straylight prevents performing observations and monitoring is not feasible. They correspond to the epochs in which

the Sun angle is smaller than 20 deg. As shown in Fig. 22, the peak of detections is reached during the activity peak of the Geminids. During such peak more than 250 impact flashes (from both the Geminids and the sporadic background) are expected to be observed thanks to the favorable Moon illumination conditions achieved by the selected quasi-halo orbit (Cipriano et al., 2018).

The individual contribution of each source is presented in the bar plot of Fig. 24. The average number of impacts is indicated by the height of the bar, while the standard deviation from the mean is represented by red error bars. Some sources give a small contributions, while others are never detected in any scenario.

7. Conclusion

LUMIO is a 12U XL CubeSat equipped with the LUMIO-Cam, an optical instrument capable of detecting impact flashes to continuously monitor and process the data. The mission implements a sophisticated transfer phase and orbit design, and it will make use of the most advanced COTS CubeSat technology to serve as a demonstrator for the use of CubeSats as viable, low-cost platforms for interplanetary science and exploration missions.

In this work, an overview of the mission and a prediction of its scientific outcome have been discussed. We presented the combined POE methodology devised to estimate the scientific return of the mission. An overview of the lunar meteoroid environment model used in the
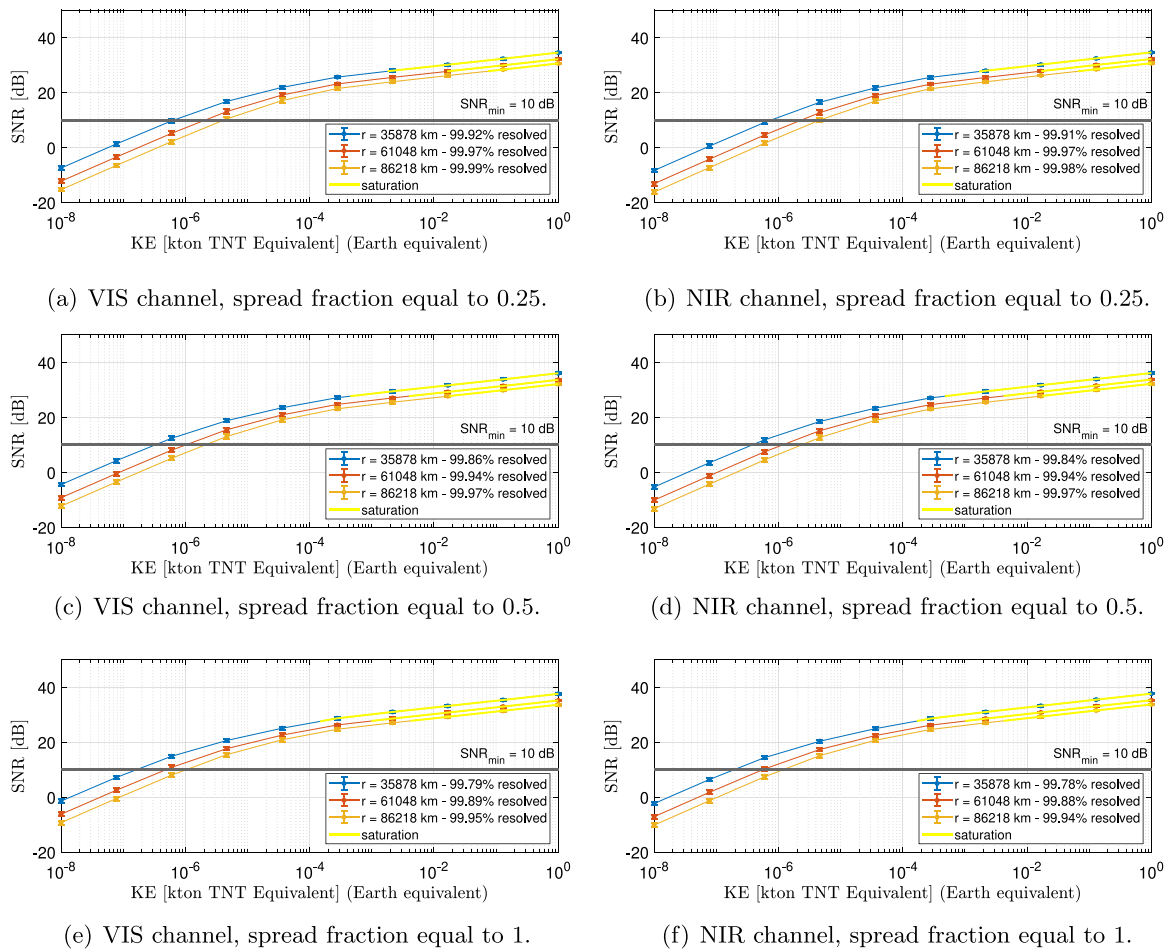
(a) VIS channel, spread fraction equal to 0.25.

(b) NIR channel, spread fraction equal to 0.25.

(c) VIS channel, spread fraction equal to 0.5.

(d) NIR channel, spread fraction equal to 0.5.

(e) VIS channel, spread fraction equal to 1.

(f) NIR channel, spread fraction equal to 1.

Fig. 20. Radiometric analysis about impact flash detection accounting for straylight, Sun angle equal to 90 deg. The SNR as a function of the impact kinetic energy in Earth equivalent is drawn for significant cases. The plots show how the SNR varies in the two channels for the three different cases of flash impact peak location within the central pixel of the detector. In each chart the SNR for different distances from the Moon of LUMIO is plotted. In yellow are identified the impact kinetic energies that saturate the detectors. The black horizontal line marks the conservative threshold of minimum SNR of 10 dB. The legends contain information about the percentage of detected impacts that do not saturate the LUMIO-Cam. Gain G fixed at 10. For each given impact kinetic energy, 1000 impacts have been simulated. Semi-log scale plots.

numerical simulation has been provided. The modeling of the LUMIO-Cam and the considered noise sources has been detailed. Results of the radiometric analysis (both neglecting and accounting for straylight noise) and the integrated POE analysis have been presented.

The radiometric analysis outcome confirms the design of the LUMIO-Cam and the satisfaction of the payload functional requirements. To maximize the kinetic energy range detected by the LUMIO-Cam and mitigate the bleeding effect, proper values of the gain have been selected for both VIS and NIR channels as a function of the LUMIO–Moon distance. The performance degradation due to straylight noise has been assessed, proving that a 150 mm baffle is long enough to grant good performance when the Sun angle is between 20 deg and 90 deg. The likely energy and temporal distributions, and the expected rate of detected meteoroid impacts have been reported. According to the current mission timeline, results suggest that LUMIO could observe the Geminids and detect more than 6000 impacts per day in the kinetic energy range at Earth of $[10^{-6}, 10^{-1}]$ kton TNT Equivalent during the peak of the shower.

Finally, the scientific return of LUMIO has been compared against the current knowledge. The comparison highlights the promising contribution of the mission. In fact, LUMIO has the potential to refine information about the meteoroid population in the equivalent impact kinetic energy range at Earth of $[10^{-6}, 10^{-4}]$ kton TNT Equivalent. The mission is expected to fill the knowledge gap in the low-energy range $[10^{-4}, 10^{-1}]$ kton TNT Equivalent (see Fig. 1). Performing meteoroids

detection with LUMIO may remarkably advance our current knowledge of meteoroid models in the solar system.

Declaration of competing interest

The authors declare that they have no known competing financial interests or personal relationships that could have appeared to influence the work reported in this paper.

Data availability

Data will be made available on request.
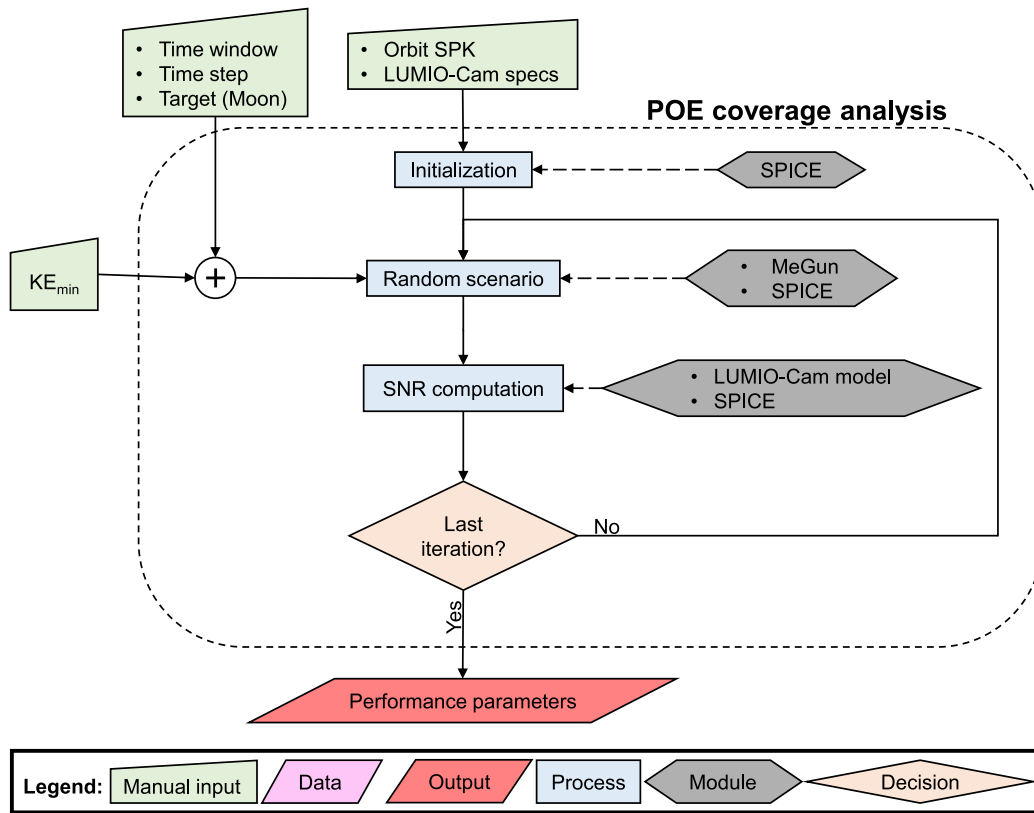
Fig. 21. Schematic representation of the POE coverage analysis methodology.
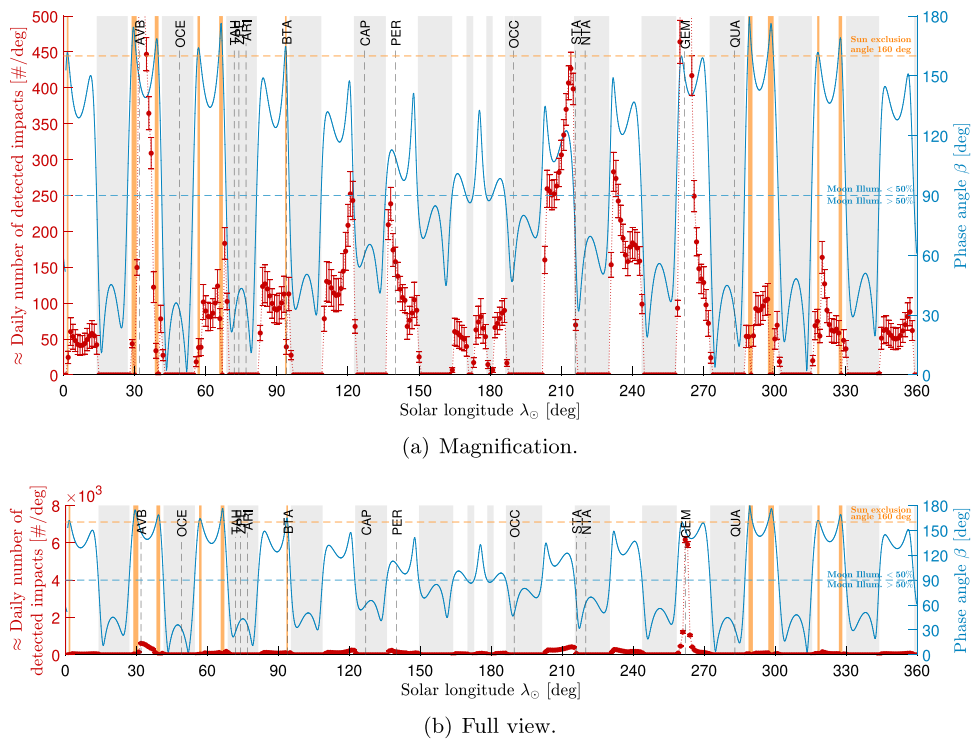

(a) Magnification.

(b) Full view.

Fig. 22. Estimation of the temporal distribution of detected lunar impacts of LUMIO lunar CubeSat. On the left *y*-axis, the approximately daily number of impacts in 1 deg bins of solar longitude (the red dots joined with the dotted red line). KE ≥ 10^{-6} kton TNT Equivalent, Earth equivalent. Results obtained from 1000 runs. On the right *y*-axis, the phase angle β (the blue solid line). The horizontal dashed blue line marks the phase angle at which Moon illumination is equal to 50%. The horizontal dashed orange line marks the phase angle corresponding to the Sun exclusion angle. The gray shaded areas highlight the epochs in which monitoring is unfeasible due to the elevated Moon illumination. The orange shaded areas highlight the epochs in which monitoring is unfeasible due to the large quantity of straylight coming from the Sun. The vertical dashed black lines are the solar longitudes at which activity periods of some major showers peak.
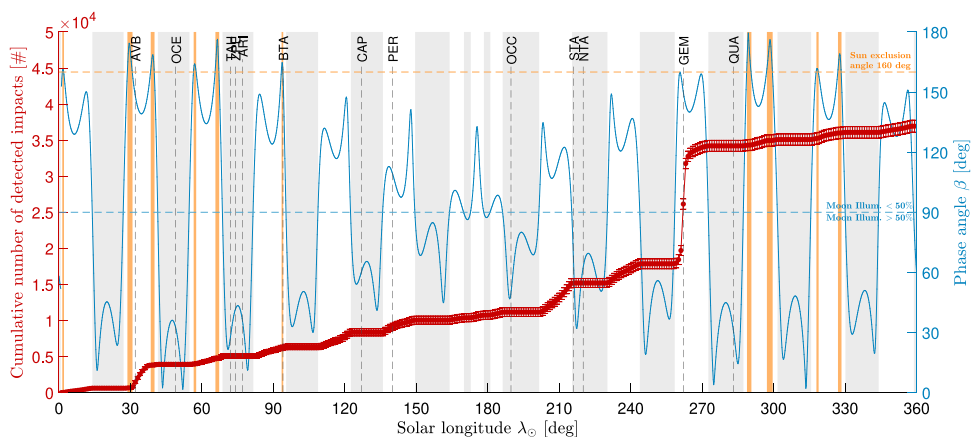
Fig. 23. Estimation of the cumulative temporal distribution of detected lunar impacts of LUMIO lunar CubeSat. On the left *y*-axis, the cumulative number of impacts in 1 deg bins of solar longitude (the red dots joined with the dotted red line). KE $\geq 10^{-6}$ kton TNT Equivalent, Earth equivalent. Results obtained from 1000 runs. On the right *y*-axis, the phase angle β (the blue solid line). The horizontal dashed blue line marks the phase angle at which Moon illumination is equal to 50%. The horizontal dashed orange line marks the phase angle corresponding to the Sun exclusion angle. The gray shaded areas highlight the epochs in which monitoring is unfeasible due to the elevated Moon illumination. The orange shaded areas highlight the epochs in which monitoring is unfeasible due to the large quantity of straylight coming from the Sun. The vertical dashed black lines are the solar longitudes at which activity periods of some major showers peak.

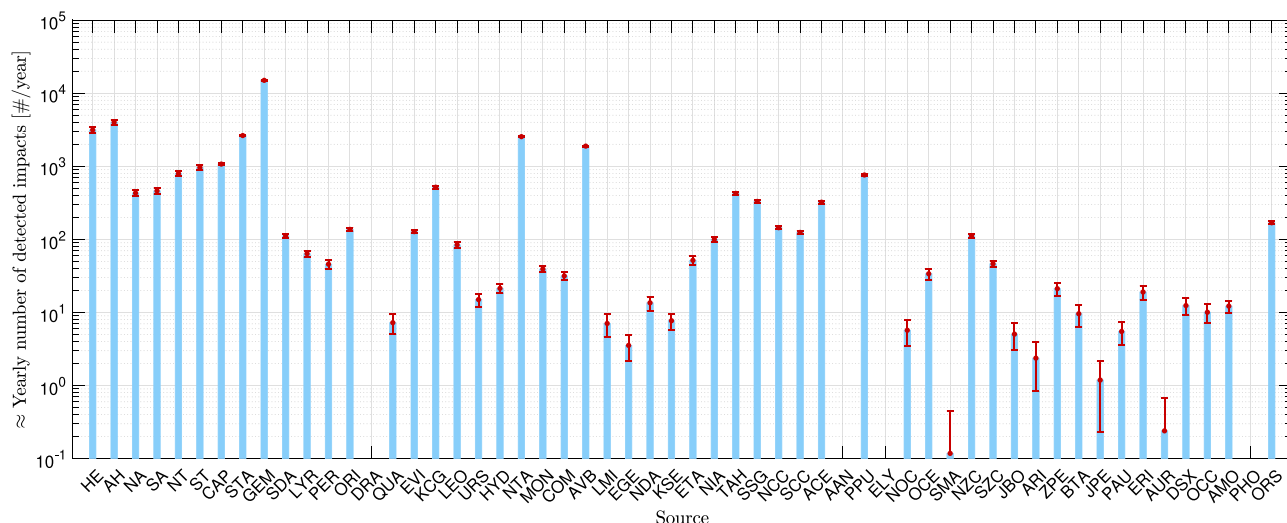**Fig. 24.** Number of detected lunar impacts by LUMIO lunar CubeSat split by source. Number of detections on the *y*-axis. Each bar is labeled with the shower IAU code or the sporadic source name tag (Merisio and Topputo, 2022). On top of each bar, there are the error bars representing the standard deviation from the average value. KE $\geq 10^{-6}$ kton TNT Equivalent, Earth equivalent. Results obtained from 1000 runs. Semi-logarithmic scale plots, logarithmic scale on *y*-axis.

References

Acton, C., Bachman, N., et al., 2018. A look towards the future in the handling of space science mission geometry. Planet. Space Sci. 150, 9–12. http://dx.doi.org/10.1016/j.pss.2017.02.013.

Acton, Jr., C.H., 1996. Ancillary data services of NASA's navigation and ancillary information facility. Planet. Space Sci. 44 (1), 65–70. http://dx.doi.org/10.1016/0032-0633(95)00107-7.

Avdellidou, C., Munaibari, E., et al., 2021. Impacts on the Moon: Analysis methods and size distribution of impactors. Planet. Space Sci. 200, 105201. http://dx.doi.org/10.1016/j.pss.2021.105201.

Babadzhanov, P.B., Kokhirova, G.I., 2009. Densities and porosities of meteoroids. Astron. Astrophys. 495 (1), 353–358. http://dx.doi.org/10.1051/0004-6361:200810460.

Bellot Rubio, L.R., Ortiz, J.L., et al., 2000. Luminous efficiency in hypervelocity impacts from the 1999 lunar Leonids. Astrophys. J. Lett. 542 (1), L65–L68. http://dx.doi.org/10.1086/312914.

Bonanos, A.Z., Avdellidou, C., et al., 2018. NELIOTA: First temperature measurement of lunar impact flashes. Astron. Astrophys. 612, A76. http://dx.doi.org/10.1051/0004-6361/201732109.

Bonanos, A.Z., Xilouris, M., et al., 2015. NELIOTA: ESA's new NEO lunar impact monitoring project with the 1.2m telescope at the national observatory of Athens. In: Proceedings of the International Astronomical Union, Vol. 10. (S318), pp. 327–329. http://dx.doi.org/10.1017/S1743921315006973.

Bouley, S., Baratoux, D., et al., 2012. Power and duration of impact flashes on the Moon: Implication for the cause of radiation. Icarus 218 (1), 115–124. http://dx.doi.org/10.1016/j.icarus.2011.11.028.

Brown, P., Spalding, R.E., et al., 2002. The flux of small near-Earth objects colliding with the Earth. Nature 420 (6913), 294–296. http://dx.doi.org/10.1038/nature01238.

Brown, P., Weryk, R.J., et al., 2008. A meteoroid stream survey using the Canadian meteor orbit radar: I. methodology and radiant catalogue. Icarus 195 (1), 317–339. http://dx.doi.org/10.1016/j.icarus.2007.12.002.

Brown, P., Wong, D.K., et al., 2010. A meteoroid stream survey using the Canadian meteor orbit radar: II: Identification of minor showers using a 3D wavelet transform. Icarus 207 (1), 66–81. http://dx.doi.org/10.1016/j.icarus.2009.11.015.

Cahill, J., Speyerer, E.J., et al., 2021. Assessing the present-day impact flux to the lunar surface via impact flash monitoring and its implications for sustained lunar exploration. Bull. AAS 53 (4), http://dx.doi.org/10.3847/25c2cfeb.68db91c2.

Ceplecha, Z., Borovička, J., et al., 1998. Meteor phenomena and bodies. Space Sci. Rev. 84 (3), 327–471. http://dx.doi.org/10.1023/A:1005069928850.

Cervone, A., Topputo, F., et al., 2022. LUMIO: A CubeSat for observing and characterizing micro-meteoroid impacts on the lunar far side. Acta Astronaut. 195, 309–317. http://dx.doi.org/10.1016/j.actaastro.2022.03.032.

Cipriano, A.M., Dei Tos, D.A., et al., 2018. Orbit design for LUMIO: The lunar meteoroid impacts observer. Front. Astron. Space Sci. 5, 29. http://dx.doi.org/10.3389/fspas.2018.00029.

Cohen, B.A., Hayne, P.O., et al., 2020. Lunar flashlight: Illuminating the lunar south pole. IEEE Aerosp. Electron. Syst. Mag. 35 (3), 46–52. http://dx.doi.org/10.1109/maes.2019.2950746.

Franzese, V., Di Lizia, P., et al., 2019. Autonomous optical navigation for the lunar meteoroid impacts observer. J. Guid. Control Dyn. 42 (7), 1579–1586. http://dx.doi.org/10.2514/1.g003999.

Grün, E., Zook, H.A., et al., 1985. Collisional balance of the meteoritic complex. Icarus 62.

Hughes, D.W., 1987. P/Halley dust characteristics-A comparison between Orionid and Eta Aquarid meteor observations and those from the flyby spacecraft. Astron. Astrophys. 187, 879–888. http://dx.doi.org/10.1007/978-3-642-82971-0_149.

Jenniskens, P., 1994. Meteor stream activity I. The annual streams. Astron. Astrophys. 287, 990–1013.

Jenniskens, P., Jenniskens, P.M.M., 2006. Meteor Showers and their Parent Comets. Cambridge University Press, pp. 585–766.

Jenniskens, P., Jopek, T.J., et al., 2009. On how to report new meteor showers. Ongoing Meteor Work 19.

Jenniskens, P., Nénon, Q., et al., 2016a. CAMS confirmation of previously reported meteor showers. Icarus 266, 355–370. http://dx.doi.org/10.1016/j.icarus.2015.08.014.

Jenniskens, P., Nénon, Q., et al., 2016b. CAMS newly detected meteor showers and the sporadic background. Icarus 266, 384–409. http://dx.doi.org/10.1016/j.icarus.2015.11.009.

Jenniskens, P., Nénon, Q., et al., 2016c. The established meteor showers as observed by CAMS. Icarus 266, 331–354. http://dx.doi.org/10.1016/j.icarus.2015.09.013.

Koschny, D., McAuliffe, J., 2009. Estimating the number of impact flashes visible on the Moon from an orbiting camera. Meteorit. Planet. Sci. 44 (12), 1871–1875. http://dx.doi.org/10.1111/j.1945-5100.2009.tb01996.x.

Liakos, A., Bonanos, A.Z., et al., 2020. NELIOTA: Methods, statistics, and results for meteoroids impacting the Moon. Astron. Astrophys. 633, A112. http://dx.doi.org/10.1051/0004-6361/201936709.

Madiedo, J.M., Ortiz, J.L., et al., 2015. Analysis of Moon impact flashes detected during the 2012 and 2013 Perseids. Astron. Astrophys. 577 (May), A118. http://dx.doi.org/10.1051/0004-6361/201525656.

Merisio, G., Giordano, C., et al., 2020. Predicting the scientific outcome of the LUMIO lunar CubeSat. In: 71st International Astronautical Congress. IAC 2020.

Merisio, G., Topputo, F., 2022. Present-day model of lunar meteoroids and their impact flashes for LUMIO mission. Icarus 115180. http://dx.doi.org/10.1016/j.icarus.2022.115180.

Oberst, J., Christou, A., et al., 2012. The present-day flux of large meteoroids on the lunar surface–a synthesis of models and observational techniques. Planet. Space Sci. 74 (1), 179–193. http://dx.doi.org/10.1016/j.pss.2012.10.005.

Oguri, K., Oshima, K., et al., 2020. EQUULEUS trajectory design. J. Astronaut. Sci. 67 (3), 950–976. http://dx.doi.org/10.1007/s40295-019-00206-y.

Ortiz, J.L., Aceituno, F.J., et al., 2006. Detection of sporadic impact flashes on the Moon: Implications for the luminous efficiency of hypervelocity impacts and derived terrestrial impact rates. Icarus 184 (2), 319–326. http://dx.doi.org/10.1016/j.icarus.2006.05.002.

Ortiz, J.L., Madiedo, J.M., et al., 2015. Lunar impact flashes from Geminids: Analysis of luminous efficiencies and the flux of large meteoroids on Earth. Mon. Not. R. Astron. Soc. 454 (1), 344–352. http://dx.doi.org/10.1093/mnras/stv1921.

Poghosyan, A., Golkar, A., 2017. CubeSat evolution: Analyzing CubeSat capabilities for conducting science missions. Prog. Aerosp. Sci. 88, 59–83. http://dx.doi.org/10.1016/j.paerosci.2016.11.002.

Puig-Suari, J., Turner, C., et al., 2001. CubeSat: the development and launch support infrastructure for eighteen different satellite customers on one launch. In: AIAA/USU Conference on Small Satellites.

Raab, H., 2002. Detecting and measuring faint point sources with a CCD. In: Proceedings of Meeting on Asteroids and Comets in Europe. MACE.

Suggs, R.M., Moser, D.E., et al., 2014. The flux of kilogram-sized meteoroids from lunar impact monitoring. Icarus 238 (Supplement C), 23–36. http://dx.doi.org/10.1016/j.icarus.2014.04.032.

Walker, R., Binns, D., et al., 2018. Deep-space CubeSats: Thinking inside the box. Astron. Geophys. 59 (5), 5–24. http://dx.doi.org/10.1093/astrogeo/aty232.

Yanagisawa, M., Uchida, Y., et al., 2021. Low dispersion spectra of lunar impact flashes in 2018 Geminids. Planet. Space Sci. 195, 105131. http://dx.doi.org/10.1016/j.pss.2020.105131.